Construction and Building Materials 423 (2024) 135800

Contents lists available at ScienceDirect

Construction and Building Materials

journal homepage: www.elsevier.com/locate/conbuildmat

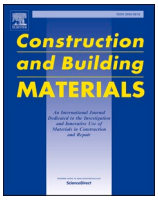

Lightweight ambient-cured geopolymer composite with expanded clay: quasi-static and dynamic properties

Zhixing Li [a], Wensu Chen [a,*], Zhiqiang Yin [b], Mizan Ahmed [a], Hong Hao [c,a,**]

[a] Center for Infrastructural Monitoring and Protection, School of Civil and Mechanical Engineering, Curtin University, Australia
[b] School of Mining and Safety, Anhui University of Science and Technology, China
[c] Earthquake Engineering Research & Test Center, Guangzhou University, China

ARTICLE INFO

Keywords:
Lightweight Geopolymer Composite (LWGPC)
Expanded clay (EC)
Quasi-static properties
Dynamic tests
Strain rate effects
Energy absorption capacities

ABSTRACT

The increased awareness of sustainability and concerns about global warming have prompted the construction industry to explore green sustainable materials such as geopolymer composites as an eco-friendly alternative to ordinary Portland cement (OPC). This study developed ambient-cured lightweight geopolymer composites (LWGPCs) by incorporating different volume fractions of expanded clay (EC). The physical and quasi-static characteristics of LWGPCs with various EC contents were investigated. Empirical formulae for the quasi-static compressive and splitting tensile strength, as well as the elastic modulus of LWGPCs were proposed. A Ø 100-mm split Hopkinson pressure bar (SHPB) system was employed to investigate the dynamic compressive and splitting tensile properties of LWGPCs. The failure processes and failure patterns of LWGPCs, as well as the stress–strain curves and the energy absorption capacities under different strain rates were compared. Based on the testing results, empirical formulae of the DIF (dynamic increase factor) for LWGPCs compressive and split tensile strength as well as the energy absorption capacities were proposed. This study offers valuable insights into the material performance of ambient-cured LWGPCs with EC as sustainable materials under quasi-static and dynamic loading, paving the way for further developing and application of lightweight and sustainable engineering materials in construction.

1. Introduction

With the development of the construction industry, the demand for concrete, as the most prevalent building material, has been continually increasing. Ordinary Portland cement (OPC) is widely used as a fundamental component in conventional concrete around the world. As estimated, OPC production has been increasing at an annual rate of 9 % owing to economic development, population increase and urbanization [1]. The environmental issues caused by OPC production are significant, as it releases large quantities of carbon dioxide (CO_2) due to the calcination of non-renewable resources such as limestone, gypsum, and fossil fuels. OPC production accounts for approximately 7 % of total industrial energy consumption and is responsible for 5–9 % of total global CO_2 emissions [2]. Meanwhile, the environmental challenges resulting from industrial waste materials are intensifying in the wake of global urbanization and industrialization [3]. Therefore, the escalating environmental impact is fostering an urgent demand for sustainable alternatives to OPC.

In recent decades, geopolymer, synthesized by reacting aluminosilicate precursors with alkaline activators, has emerged as an eco-friendly alternative to conventional cementitious materials [4]. Industrial by-products, such as fly ash (FA) and slag, as well as metakaolin are viable binder materials for producing geopolymer. Metakaolin is obtained from natural clays (kaolin) through calcination at moderate temperatures [5]. Previous studies have investigated the properties of metakaolin-based geopolymer concrete [5–8]. It was reported that metakaolin-based geopolymer exhibited superior compressive strength and thermal stability with low shrinkage as compared to conventional cement concrete. Over the last several decades, with the global push towards sustainable development, there has been a requirement to minimize the use of natural resources. Furthermore, the rise of global urbanization and industrialization has increased the discharge of industrial hazardous solid wastes, such as FA and slag, posing environmental challenges [3]. Therefore, in this study, FA and slags were used

* Corresponding author.
** Corresponding author at: Center for Infrastructural Monitoring and Protection, School of Civil and Mechanical Engineering, Curtin University, Australia.
E-mail addresses: wensu.chen@curtin.edu.au (W. Chen), hong.hao@curtin.edu.au (H. Hao).

https://doi.org/10.1016/j.conbuildmat.2024.135800
Received 10 December 2023; Received in revised form 12 February 2024; Accepted 10 March 2024
Available online 20 March 2024

as binder materials to produce geopolymer. Compared to OPC, geopolymer production can lead to a significant reduction of up to 80 % in greenhouse gas emissions and also requires less energy consumption [9–11]. Consequently, geopolymers are gaining increasing attention due to their potential to reduce carbon footprints, provide high strength and durability, among other desirable properties [12].

The construction industry exhibits considerable interest in lightweight concrete (LWC) because of its superior strength-to-weight ratio [13]. LWC is defined to have a density of 800–2000 kg/m^3 with various strength [14], which can be produced by substituting natural aggregate either partially or completely with lightweight aggregate (LWA) based on the demand of density and strength. Lightweight geopolymer composites (LWGPCs) have gained increased attention by using geopolymer as the matrix material due to their enhanced durability, reduced environmental footprint, and sustainable attributes [15]. Lightweight aggregates, including materials like expanded clay, slate, perlite, and pumice [16], have been used to produce LWC for various applications. Expanded clay (EC) is produced as a porous material with a spherical shape [17]. Notably, the EC aggregate demonstrates higher strength and better resistance to segregation compared to most of other lightweight aggregates [18]. Its porous feature attributes lightweight characteristics coupled with exceptional thermal and acoustic insulation properties as well as improved fire resistance [19]. LWC with EC has been widely used in various applications, including lightweight bricks and blocks [20], masonry plaster and mortar [21,22], structural LWC components [23–25] and filling material [26].

Previous studies have developed LWGPCs using EC as a lightweight aggregate, while most of them have concentrated the quasi-static characteristics. For example, Priyanka et al. [27] investigated FA-based LWGPC activated by sodium hydroxide (NaOH) with molarity of 8 mol/L (8 M) and sodium silicate (Na_2SiO_3) solution, revealing a compressive strength range of 26.6–43.4 MPa with a density between 1550 and 2030 kg/m^3. Abdulkareem et al. [28] produced FA-based LWGPC with EC activated by 12 M (mol) NaOH and Na_2SiO_3 solution, achieving a compressive strength of 18.86 MPa with a density of 1438 kg/m^3. Yang et al. [29] developed slag-based LWGPCs using Na_2SiO_3 solution as alkaline activator and reported a compressive strength range of 26.5–39.6 MPa at a density range of 1420–1974 kg/m^3. FA and slag-based LWGPCs with a density of 1132–2177 kg/m^3 achieved a compressive strength of 19.5–35 MPa [30]. It was found that LWGPCs had superior durability, sound isolation, thermal insulation and fire resistance in comparison to normal-weight concrete. Additionally, the studies conducted on LWGPC with EC demonstrated several advantages, including enhanced durability and workability as well as lesser shrinkage [19].

Limited studies have investigated the dynamic compressive properties of LWC using various lightweight aggregates. Bai et al. [31] investigated the behaviour of LWC incorporating ceramsite aggregate at the strain rates of 37.60–126.43 s^{-1}. The ceramsite aggregate had a density of 510 kg/m^3 and compressive strength over 1.5 MPa. It was reported that the dynamic properties of LWC with ceramsite aggregate, including strength, impact toughness and energy absorption capacities, were quite sensitive to strain rates. Wu et al. [32] conducted dynamic tests on LWC with shale-ceramsite subjected to impact loads at strain rates ranging from 19 to 127 s^{-1}. Du et al. [33] undertook an experimental investigation into the response of expanded-shale LWC at strain rates of 34.3–109.3 s^{-1}. Prior studies also examined the dynamic compressive properties of new LWGPCs with expanded polystyrene and coated expanded polystyrene [34,35]. LWC contains various components such as matrix, aggregates, and porous LWAs, as well as their interfaces. Under low strain rate loading, initial cracks tend to form and propagate along weaker sections, causing the specimen to predominantly fracture into large pieces. As the strain rate increases, more internal cracks develop from discontinuities and propagate rapidly. As a result, the specimen shatters into numerous small pieces. This damage mechanism under dynamic loading highlights the effect of strain rate on the dynamic properties of materials. However, to date, no study has delved into the dynamic compressive and splitting tensile behaviours of LWGPCs incorporated with EC.

In this study, novel ambient-cured LWGPCs incorporated with EC in volumetric proportions of 10 %, 20 %, and 30 % were developed as sustainable lightweight materials. This study investigated and quantified physical, quasi-static and dynamic properties of LWGCs for their practical applications in construction. Dynamic compressive and split tensile tests on the LWGPCs were conducted by using a Ø100-mm Split Hopkinson Pressure Bar (SHPB) to analyse their dynamic behaviour dependent on strain rate. The strain-rate sensitivity of the LWGPCs was evaluated by the dynamic increase factors. Additionally, the physical and mechanical attributes of LWGPCs were also compared with those of a plain geopolymer mortar (GM) from the authors' previous study [35]. The study also proposed empirical formulae for compressive DIF (CDIF) and tensile DIF (TDIF) and the energy absorption capacities at varying strain rates.

2. Experimental programme

2.1. Materials, mixes, and specimen preparation

The physical properties and suppliers of the raw materials are summarized in Table 1, which were consistent with the authors' previous study [35]. The binder materials included low-calcium FA, classified as Class F as per ASTM C618 [36], and construction-grade blast furnace slag. The alkaline activator consisted of a 8 M (molarity = 8 mol/L) sodium hydroxide (NaOH) solution and D-grade sodium silicate (Na_2SiO_3) solution. NaOH solution was prepared 24 h prior to mixing to allow the dissipation of heat from the exothermic reaction. Silica sand was used as the fine aggregate. EC, with a diameter of 4–6 mm and a specific gravity of 0.77, was employed as LWA. It had an aggregate crushing strength of 8 MPa and a water absorption of around 10 % [37]. As shown in Fig. 1, the spherical EC featured a closed surface with micro-pores inside its structure.

The typical governing parameters to determine the strength and workability of geopolymer include binder to alkaline activator ratio, FA to slag ratio, Na_2SiO_3 to NaOH ratio, curing conditions as well as type and source of aluminosilicate material. In this study, all these parameters were kept unchanged, except the volume of EC and sand. The mix proportions of GM were determined based on the authors' previous study [38]. For GM, the mass ratios of binder materials to sand were set at 0.625. The binder to alkaline activator ratio was 2.50. Binder materials were fixed at 75 % FA and 25 % slag. The Al_2O_3/SiO_2 ratio in the mix design was approximately 0.492. The alkaline activator was prepared using Na_2SiO_3 to NaOH solutions at a mass ratio of 2.50. The Na_2O/H_2O ratio was around 0.41. EC was incorporated into the GM by replacing sand at three volume ratios of 10 %, 20 %, and 30 %, corresponding to 12.62 %, 25.24 % and 37.86 % in weight of sand, which were labelled as EC-10, EC-20, and EC-30, respectively. The specific mix proportions of the GM and LWGPC with varying EC volume fractions are

Table 1
Physical properties of raw materials.

Material	Specific gravity	Median particle size	Fineness modulus	Supplier
Expanded clay	0.77	4–6 mm	-	Liapor, Perth
Silica sand	2.65	1.2 mm	2.77	Hanson Construction Materials, Sydney
Fly ash (Class F)	2.40	9.7 μm	-	Gladstone Power Station, Queensland
Slag	3.15	11.5 μm	-	BGC Cement, Perth
NaOH (8 M)	1.28	-	-	Chem-Supply Pty Ltd, Adelaide
Na_2SiO_3 (D grade)	1.53	-	-	PQ-Australia, Melbourne

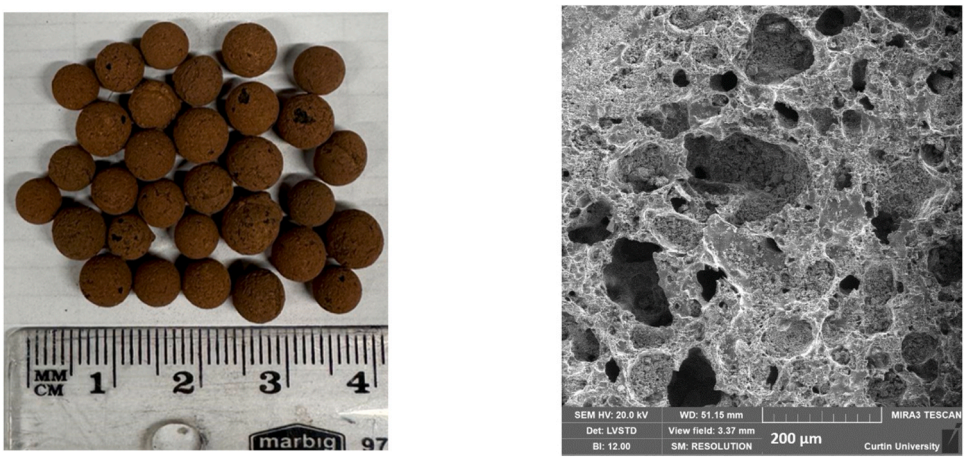

(a) (b)

Fig. 1. Lightweight expanded clay: (a) photographs and (b) cross-section SEM image.

detailed in Table 2.

The mixing process of LWGPC is outlined in Fig. 2 using a pan-type mixer. The alkaline activating solution by combining NaOH and Na_2SiO_3 solutions was prepared at least 30 minutes prior to mixing. First, dry ingredients such as FA, slag, and sand were blended for three minutes at a speed of 70 ± 5 rpm. After that, the alkaline activator was gradually added to the mixer to form the geopolymer mortar. Then, EC was added and mixed for three minutes at a mixing speed of 70 ± 5 rpm, ensuring the uniform distribution of EC throughout the geopolymer matrix. The blended mixtures were then cast into cylindrical molds with dimensions of Ø100 ×200 and Ø150 ×300. To minimize the presence of entrapped air, the mixtures underwent a vibration period of 30 seconds. The molded specimens were cured under ambient conditions for 24 h, maintaining a temperature of 22 ± 2 °C and relative humidity of 50 ± 5 %, in accordance with ASTM C330/C330M [39]. After demolding, the specimens were sealed with plastic wrap and then left to cure under ambient conditions for 28 days before testing. Fig. 3 illustrates the uniform dispersion of EC particles in three LWGPC specimens.

2.2. Testing method and equipment

2.2.1. Scanning electron microscopy (SEM) analysis

The porous structure of EC and the interfacial transition zone (ITZ) between the EC and the geopolymer matrix were studied using a MIRA3 TESCAN Scanning Electron Microscope (SEM), as per ASTM C1723 [40]. Samples measuring 10 mm × 10 mm × 10 mm were extracted from the tested cylindrical specimens after a 28-day curing period. The SEM analysis was conducted under low vacuum modes, with an accelerating voltage of 10.0 kV and a beam intensity (BI) of 10.0.

2.2.2. Density and workability

The fresh density of the mixtures was measured as per ASTM C1688 [41], with the mean value determined from three specimens of each configuration. Additionally, the influence of EC on the workability of the mixtures was assessed in accordance with ASTM C1437 [42]. Two flow table tests were executed directly after mixing each batch.

Table 2
Mix proportions of GM and LWGPCs.

Mix proportions (kg/m^3)							
Mix design	Fly ash	Slag	NaOH	Na_2SiO_3	Sand	Expanded clay	
						Weight (kg/m^3)	Volume (%)
GM	595	105	80	200	1120	-	-
EC-10	595	105	80	200	855	57	10
EC-20	595	105	80	200	590	114	20
EC-30	595	105	80	200	325	171	30

2.2.3. Quasi-static test

The quasi-static compressive and splitting tensile tests were conducted as per ASTM C39 [43] and ASTM C496 [44], respectively, using the MCC system as depicted in Fig. 4. The equivalent loading rate was set to 0.33 MPa/min for compressive tests and 0.70 MPa/min for splitting tensile tests. The cylindrical specimens measured Ø100 ×200 mm for compressive tests and Ø150 ×300 mm for splitting tensile tests. To ensure uniform stress distribution, the specimens for the compressive tests were capped with sulfur mortar, and the specimens for the splitting tensile tests were sandwiched between the compressive platens. For each mix configuration, at least three specimens were tested.

2.2.4. Elastic modulus and Poisson's ratio

The measurements and calculations of the elastic modulus and Poisson's ratio were conducted as per ASTM C469 [45]. Longitudinal strains were captured by strain gauges aligned with the compression direction, and transverse strains were recorded from strain gauges positioned perpendicularly to the compression direction. The elastic modulus (E) and Poisson's ratio (μ) can be determined using the following equations.

$$E = (S_2 - S_1)/(\varepsilon_2 - \varepsilon_1) \quad (1)$$

where S_2 represents the stress corresponding to 40 % of the ultimate load; S_1 corresponds to the stress associated with longitudinal strain ε_1; ε_1 is equal to 0.000050; ε_2 is the longitudinal strain induced by stress S_2.

$$\mu = (\varepsilon_{t2} - \varepsilon_{t1})/(\varepsilon_2 - \varepsilon_1) \quad (2)$$

where ε_{t2} denotes the transverse strain at the mid-height of the specimen corresponding to stress S_2; ε_{t1} represents the transverse strain at the mid-height of the specimen corresponding to stress S_1. At least three tests for each mix configuration were conducted.

2.2.5. Dynamic compressive and splitting tensile tests

For the impact tests, disc-shaped specimens with a diameter of 100 mm and height of 50 mm were utilized, wherein a length-to-diameter ratio of 0.5 was employed to minimize the effects of inertia and end friction on the dynamic test results [46]. The disc-shaped specimens were cut from Ø100 × 200 cylindrical specimens. The end surfaces of the specimens were polished to ensure their parallelism and smoothness. The impact tests were executed using the Ø100-mm SHPB testing apparatus. Fig. 5 (a) and (b) show the schematic diagram and

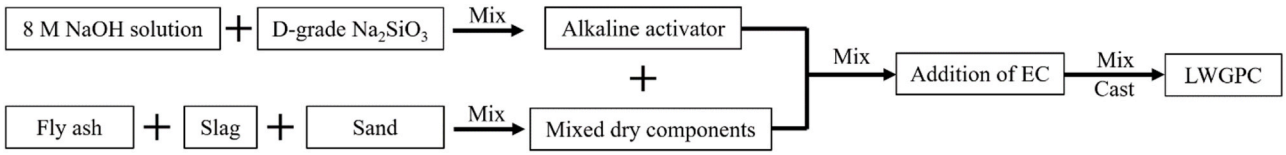

Fig. 2. Flow chart for preparation of LWGPCs.

Fig. 3. Cross-sectional images of LWGPCs.

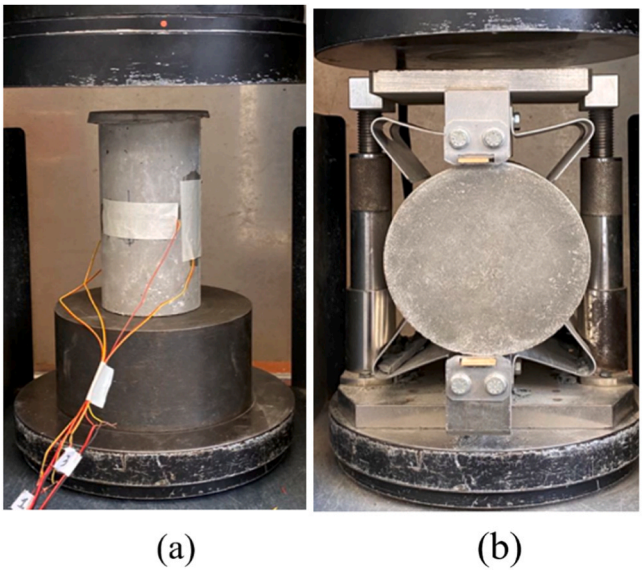

Fig. 4. Quasi-static tests set-up.

photograph of the dynamic test set-up. The apparatus comprised a striker and two pressure bars, including an incident bar and a transmitted bar, both made of stainless steel with an elastic modulus of 200 GPa, the density of 7800 kg/m^3 and a Poisson's ratio of 0.3. The strain signals were captured by the strain gauges attached to the pressure bar. The failure process was captured using a high-speed camera capable of recording at a maximum frame rate of 1,000,000 fps with an image resolution of 96 × 96 dpi. Crack-opening displacement (COD) were captured using the Digital Image Correlation (DIC) technique. In order to reduce the impact of end friction, the interface between the specimen and the pressure bars was greased. Furthermore, a circular rubber pulse shaper, 20 mm in diameter and 3 mm in thickness was affixed to the impact end of the incident bar. It was reported that the circular shaper can mitigate high-frequency oscillations in the recorded signal and facilitate the achievement of dynamic stress equilibrium [47].

To ensure the results of the SHPB test be valid, it is crucial to achieve stress equilibrium. Fig. 6 (a) illustrates a typical stress equilibrium during the dynamic test. In this study, stress equilibrium was verified for all dynamic tests by ensuring that the sum of the incident and reflected waves aligned closely with the transmitted wave.

Based on the theory of one-dimensional stress wave propagation, the dynamic stress σ, strain rate $\dot{\varepsilon}$ and strain ε of the specimens can be determined from the strain signal using the following equations [48].

$$\sigma(t) = E_b\left(\frac{A_b}{A_s}\right)\varepsilon_T(t) \tag{3}$$

$$\dot{\varepsilon}(t) = \frac{2C_0}{L}\varepsilon_R(t) \tag{4}$$

$$\varepsilon(t) = \int_0^T \dot{\varepsilon}(t)dt \tag{5}$$

where E_b, A_b and C_0 refer to the elastic modulus, cross-section area and elastic wave velocity of the pressure bars, respectively; A_s and L represent the cross-section area and length of the tested specimen, respectively; ε_T and ε_R denote the transmitted and reflected strain. Dynamic compressive strength is characterized by the peak stress. Fig. 6 (b) displays the determination of strain rate. In this study, the strain rate was determined at the moment corresponding to the peak stress, as also adopted in previous studies [34,49,50].

Dynamic splitting tensile strength (f_{td}) is proportional to the peak value of transmitted wave $\varepsilon(t)_{max}$ as expressed in Eq. (6). Thus, the corresponding stress rate ($\dot{\sigma}$) and strain rate ($\dot{\varepsilon}$) of the specimen can be determined by Eqs. (6)-(8), respectively [51].

$$f_{td} = \left(\frac{R_B^2 E_B}{R_G H_G}\right)\varepsilon(t)_{\max} \tag{6}$$

$$\dot{\sigma} = \frac{f_{td}}{t} \tag{7}$$

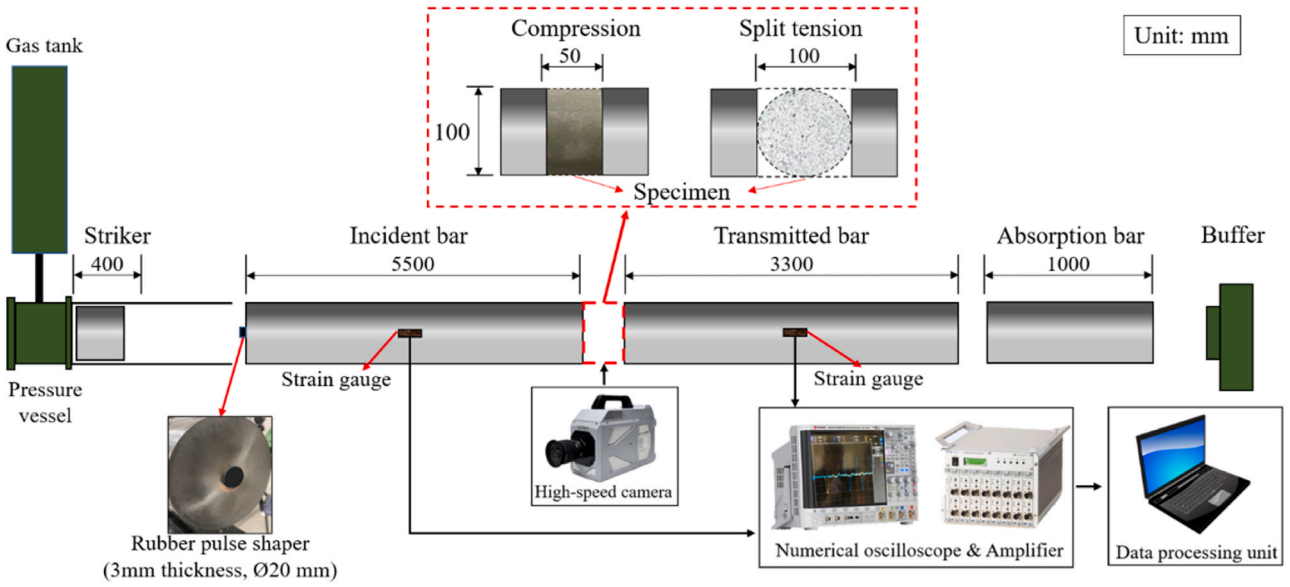

(a)

(b)

Fig. 5. (a) Schematic diagram and (b) photograph of SHPB test set-up.

$$\dot{\varepsilon} = \frac{\dot{\sigma}}{E_G} \tag{8}$$

where f_{td} is the peak dynamic split tensile strength; R_B and R_G denote the radius of the pressure bars and the specimen, respectively; E_B and E_G represent the elastic modulus of the pressure bars and the specimen, respectively; H_G is the thickness of the specimen; $\varepsilon(t)$ denotes the transmitted strain, and t is the time lag from the initiation to the peak dynamic split tensile strength.

3. Physical and quasi-static properties

3.1. Density and workability

The fresh properties of GM and LWGPCs are compared in Fig. 7. As expected, the fresh properties of LWGPCs, including density and workability, decreased as EC content increased. For instance, GM, with a density of 2204.41 kg/m^3, had a flow rate of 104.33 %. Replacing sand with EC at 10 %, 20 %, and 30 % in LWGPC led to the decreased densities of 1909.24 kg/m^3, 1719.55 kg/m^3, and 1529.89 kg/m^3, respectively. However, the workability, as evaluated by flowability, decreased by 7.04 %, 15.33 %, and 22.98 % for the LWGPC with 10 %, 20 %, and 30 % EC, respectively, compared to GM. The reduction in flowability can be attributed to the rough surface texture and increased porosity of EC. The rough surface of the EC particles created internal friction and hindered the movement of the geopolymer matrix [52]. As the proportion of EC increased, more surface area was introduced, leading to an increased amount of internal friction and reduced flowability. Additionally, the increased porosity of EC particles might have led to an increase in viscosity due to water absorption, further decreasing the flowability of the matrix [19,53].

3.2. Quasi-static compressive properties

Fig. 8 (a)–(d) display the post-failure patterns of the specimens under compression. It was observed that the GM specimen exhibited brittle

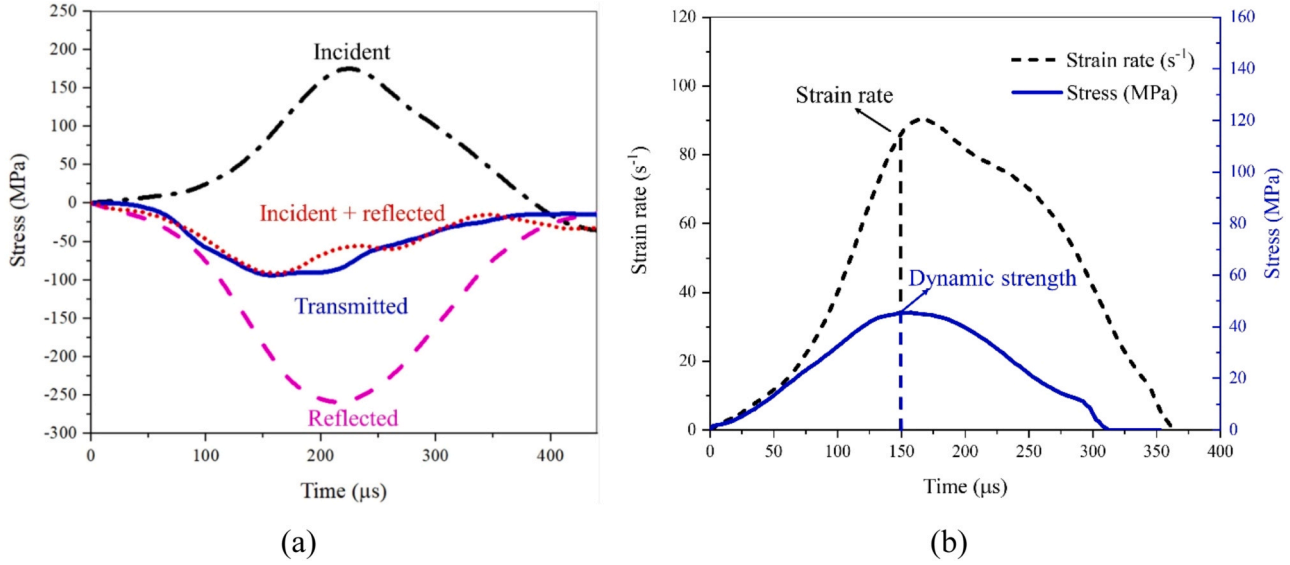

Fig. 6. Illustration of (a) stress equilibrium and (b) strain rate determination.

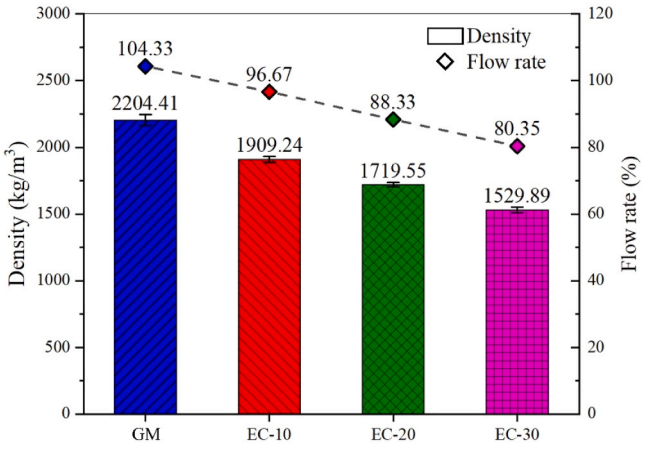

Fig. 7. Density and workability of LWGPCs with different contents of EC.

failure with an hourglass-shaped core remaining. With the increase in EC content, LWGPC specimens tended to deform gradually and fail progressively. For instance, the EC-10 specimen displayed cracks throughout its entirety, and significant lateral bulging was evident. In contrast, only half of the EC-30 specimen, starting from the top surface, showed signs of damage with fewer cracks. This finding aligns with previous studies on the influence of LWAs on LWC [54,55]. It indicates that the porous structure of EC led to a less brittle failure mode under quasi-static compression and improved energy absorption capacities.

Fig. 9 presents the mean quasi-static compressive strength for GM and LWGPCs. As expected, a decreasing trend in quasi-static compressive strength was observed with increasing volume percentages of EC. For example, when EC replaced 10 %, 20 %, and 30 % of sand by volume, the quasi-static compressive strength of the developed LWGPCs decreased by 20.57 %, 33.22 %, and 48.97 % as compared to that of GM, respectively. The quasi-static compressive strength of EC-10, EC-20 and EC-30 was 48.55 MPa, 40.81 MPa and 31.19 MPa, respectively, and their corresponding densities are given in Fig. 7. Both the density and compressive strength of the developed LWGPCs met the specifications for structural lightweight concrete, which mandate a compressive strength exceeding 17 MPa and a density range between 1120 and 1920 kg/m^3 as per ACI 213R-14 [56]. Owing to their superior strength-to-weight ratio compared to conventional lightweight concrete, LWGPCs are suitable for a range of lightweight structural applications, such as beams, slabs, roofs, floor, and marine structures [56].

Fig. 10 presents a comparison of the relationship between quasi-static compressive strength and density of LWGPCs produced in this study against the findings from previous studies on LWC with EC and LWGPC with EC. It was observed that LWGPCs developed in the current study achieved higher compressive strength for a given density compared to LWC with EC [57] and LWGPCs with EC from previous studies [27,29,30,58–61]. The mechanical properties of LWGPCs with the same density mainly depend on the types of constituents (binder and alkaline activator) and mix proportions. For instance, Priyanka et al. [27] investigated FA-based LWGPC (Concrete) made with 8 M NaOH solution and sodium silicate, achieving a compressive strength of 26.6–43.4 MPa and a density of 1550–2030 kg/m^3. Abdulkareem et al. [28] manufactured FA-based LWGPC (Mortar) with a compressive strength of 18.86 MPa and a density of 1438 kg/m^3, activated by a 12 M NaOH solution and sodium silicate. Moreover, Yang et al. [29] developed slag-based LWGPCs (Concrete) using sodium silicate as the alkaline activator. These studies employed only FA or slag as individual binder material. In contrast, the current research used FA combined with an optimal amount of slag as the binder at a ratio of 1.6 to synthesize LWGPCs. This combination, possibly due to the incorporation of slag, improved the compactness of the microstructure of geopolymer matrix and the bonding strength between EC and the matrix [62–64]. An empirical model that describes the correlation between the quasi-static compressive strength and the density of the ambient cured LWGPCs with EC, with densities ranging from 1529 to 1909 kg/m^3, is proposed as follows.

$$f_c'^{0.67} = 2.95 w_c^{1.58} 10^{-4} \ (R^2 = 0.97) \text{ for } 1529\ \text{kg/m}^3 \le w_c \le 1909\ \text{kg/m}^3 \quad (9)$$

where f_c' denotes the quasi-static compressive strength (MPa); and w_c represents the density (kg/m^3).

Fig. 11 illustrates the average values for both modulus of elasticity (MOE) and Poisson's ratio of GM and LWGPCs. As the EC content increased, the MOE of LWGPCs decreased, whereas the value of Poisson's ratio increased. For instance, the MOE and Poisson's ratio in GM were 17.82 GPa and 0.11, respectively. When 10 %, 20 %, and 30 % of sand were replaced with EC by volume, the MOE of LWGPCs decreased by 9.98 %, 24.5 %, and 34.62 % to 16.04 GPa, 13.44 GPa, and 11.65 GPa, respectively. The observed decrease could be attributed to the inherently lower stiffness of EC particles compared to the GM matrix,

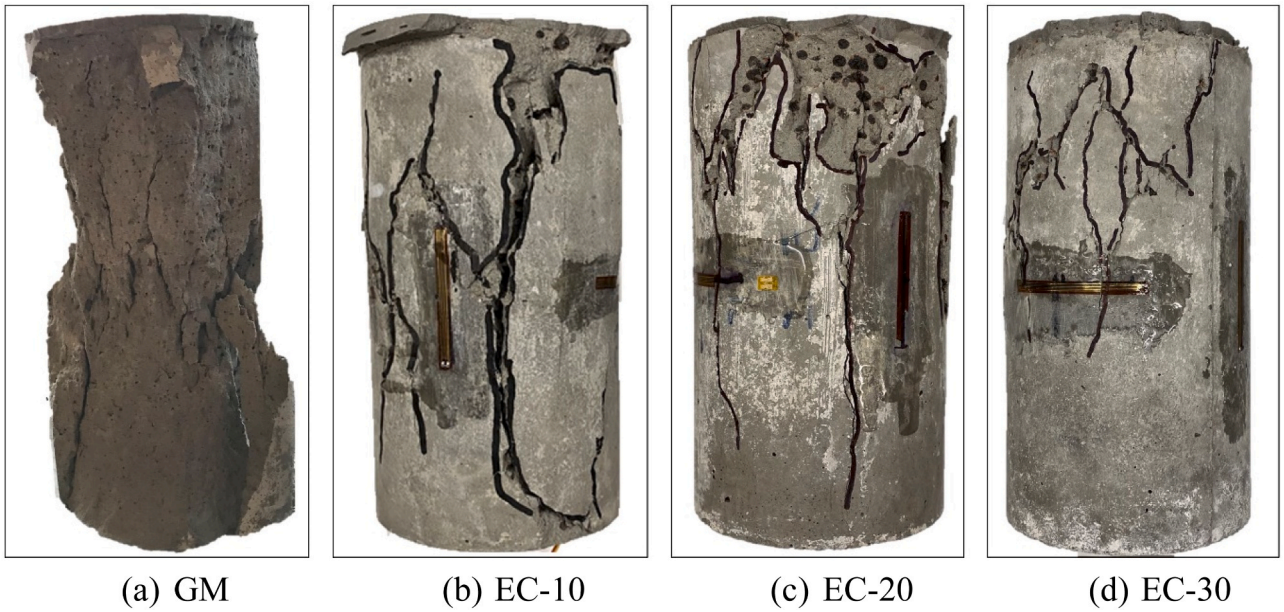

Fig. 8. Comparison of failure patterns of GM and LWGPCs under quasi-static compression.

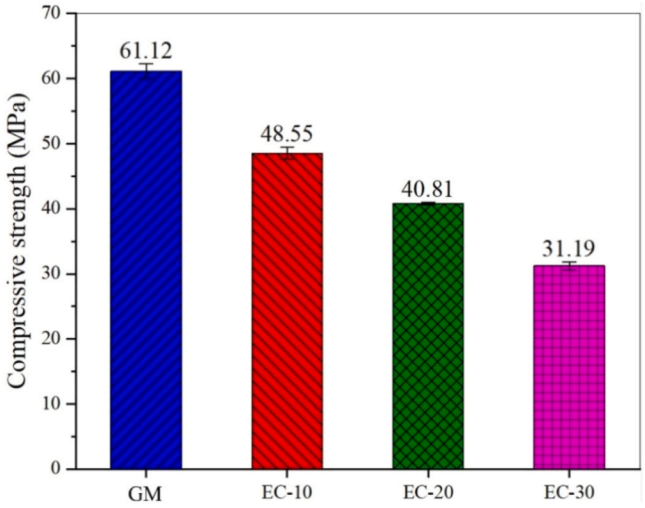

Fig. 9. Quasi-static compressive strength of GM and LWGPCs.

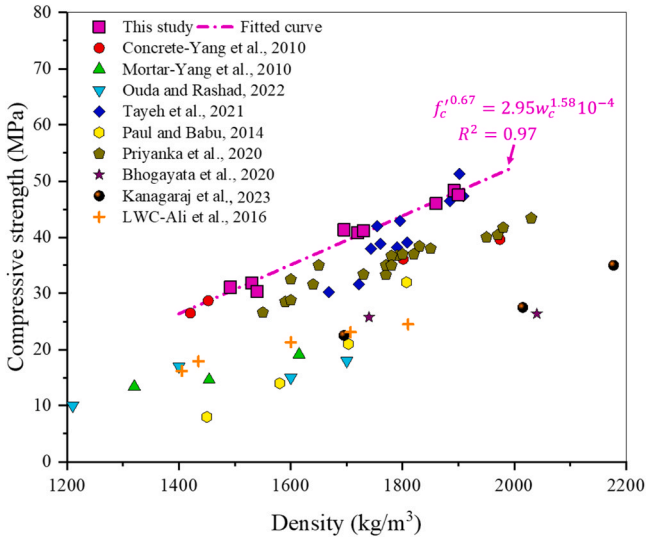

Fig. 10. Comparison of the correlation between compressive strength and density from this study and previous studies on LWC [57] and LWGPC [27,29,30,58–61].

resulting from their porous structure. It is worth noting that while the developed LWGPC exhibits a reduced modulus of elasticity in comparison to normal-weight concrete, it remains within the requirements for structural applications, specifically between 10.0 GPa and 24.0 GPa [65]. Moreover, the Poisson's ratio of LWGPCs increased by 27.2 %, 45.4 % and 72.7 % to 0.14, 0.16 and 0.19 when 10 %, 20 %, and 30 % by volume of EC was incorporated, respectively. This rise is primarily due to the greater deformability of EC as compared to sand.

The prediction of MOE for concrete-like materials is essential for the structural design [66]. Commonly used empirical models [67–74] as summarized in Table 3 were proposed to predict the MOE of concrete. Fig. 12 presents the comparison of MOE values from this study and existing models. As shown, the existing models from standards for normal-weight concrete overestimated the MOE of developed LWGPCs. It is noted that Dilli et al. [68] modified the model from CEB-FIB and ACI 363 to predict the MOE of LWC with EC, which also overestimated the MOE of LWGPCs. As reported, the LWC with the fresh density of 1710–2101 kg/m^3 was manufactured by partially replacing the natural coarse aggregate with EC. The overestimation might be because coarse aggregate was applied in the concrete composites, which possessed higher stiffness than EC. In this study, the MOE of the developed LWGPCs is proposed based on the ACI 363 model as

$$E_c = 1613\sqrt{f_c'}(w_c/2300)^{2.9} + 9869\ (\mathrm{R}^2 = 0.97)\ \text{for}\ 1529\ \mathrm{kg/m^3} \le \mathrm{wc} \le 1909\mathrm{kg/m^3} \quad (10)$$

3.3. Quasi-static splitting tensile properties

Fig. 13 displays the typical splitting failure patterns observed in both GM and LWGPCs with EC. Each specimen exhibited failure along a central crack, which aligns with the requirements specified for concrete splitting tensile tests [44]. Throughout the splitting tensile test, it was observed that the GM specimen underwent brittle failure, splitting into

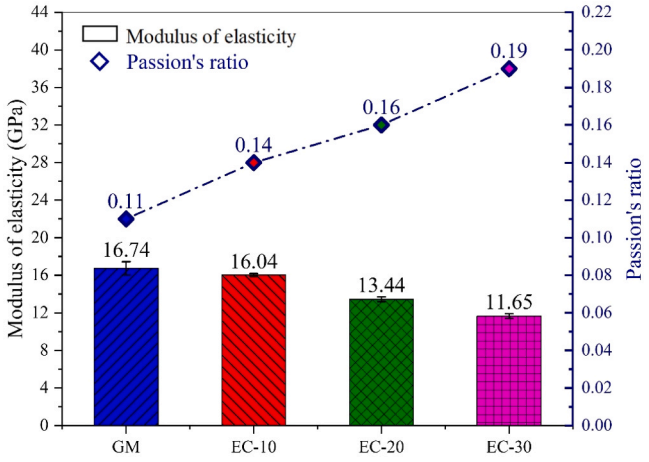

Fig. 11. Elastic modulus and Poisson's ratio of GM and LWGPCs.

Table 3
Prediction models for estimating elastic modulus and splitting tensile strength.

Model	Prediction model for E (MPa)	Prediction model for f_{st} (MPa)
ACI 363 [69]	$E_c = (3320\sqrt{f_c'} + 6900)(w_c/2300)^{1.5}$	-
CEB-FIB [70]	$E_c = 15050\sqrt[3]{f_c'/10}$ *	$f_{st} = 0.23 f_c'^{0.75}$
Modified CEB-FIB [68]	$E_c = 10750\sqrt{f_c'/10}$	-
Modified ACI 363 [68]	$E_c = 3000\sqrt{f_c'}(w_c/2300)^{3.7} + 12500$	-
ACI 318 [71]	$E_c = 0.043 w_c^{1.5}\sqrt{f_c'}$	$f_{st} = 0.42 f_c'^{0.5}$
Eurocode 2 [72]	$E_c = 22000(f_c'/10)^{0.3}(w_c/2200)^2$	$f_{st} = 0.33 f_c'^{0.75}(0.4 + \frac{0.6 w_c}{2200})$
AS 3600 [73]	-	$f_{st} = 0.36 f_c'^{0.5}$
Ahmad et al. [67]	-	$f_{st} = 0.178 f_c'^{0.75}$
Shafigh et al. [74]	-	$f_{st} = 0.20 f_c'^{0.75}$

Note: "-" not available.

two halves. In contrast, the LWGPC specimen demonstrated a more progressive failure as the amount of EC content increased. It is worth noting that EC-20 and EC-30 specimens remained intact with one main crack after reaching peak stress.

Fig. 14 (a) shows the quasi-static splitting tensile strength of GM and LWGPCs. It was observed that the splitting tensile strength decreased as the proportion of EC content increased. Specifically, GM had the splitting tensile strength of 5.21 MPa, whereas reductions of 16.70 %, 34.93 %, and 52.98 % were observed when sand was replaced by 10 %, 20 %, and 30 % EC content by volume, respectively. This reduction was primarily attributed to the highly porous structure of EC, which decreased the effective stress area as the EC volume fraction increased [67].

Fig. 14 (b) compares the splitting tensile strength predicted by the standards for LWC, previous studies on LWC [67,70–74] and the results from this study. Prediction models are summarized in Table 3. It was observed that the predicted results either underestimated or overestimated the splitting tensile strength of the developed LWGPCs. OPC-based concrete and geopolymer materials exhibit variability in their mechanical properties due to the factors such as differences in raw materials, mix proportions, and curing conditions. This inherent variability might contribute to the discrepancies in tensile strength predictions. It is essential to develop more accurate prediction models specifically for ambient-cured LWGPCs with EC. In this study, the Eurocode 2 model was modified to predict the splitting tensile strength of LWGPCs with EC as follows.

$$f_{st} = 0.75 f_c'^{0.75}\left(\frac{0.4 w_c}{2200} - 0.02\right)(R^2 = 0.97) \text{ for } 1529\text{kg}/\text{m}^3 \le w_c \le 1909\text{kg}/\text{m}^3 \quad (11)$$

The results of physical and quasi-static tests are summarised in Table 4.

3.4. Scanning electron microscopy analysis

The microstructure of concrete is an important factor in defining its material properties. Previous studies on aggregate properties and their effects on LWC have revealed that the weakest component of concrete typically determined its material strength [75]. LWA and ITZ are the weakest components, significantly impacting the mechanical and elastic properties of LWGPC [76,77]. In this study, SEM analysis was performed on LWGPCs to evaluate the ITZ between the matrix and EC for a detailed

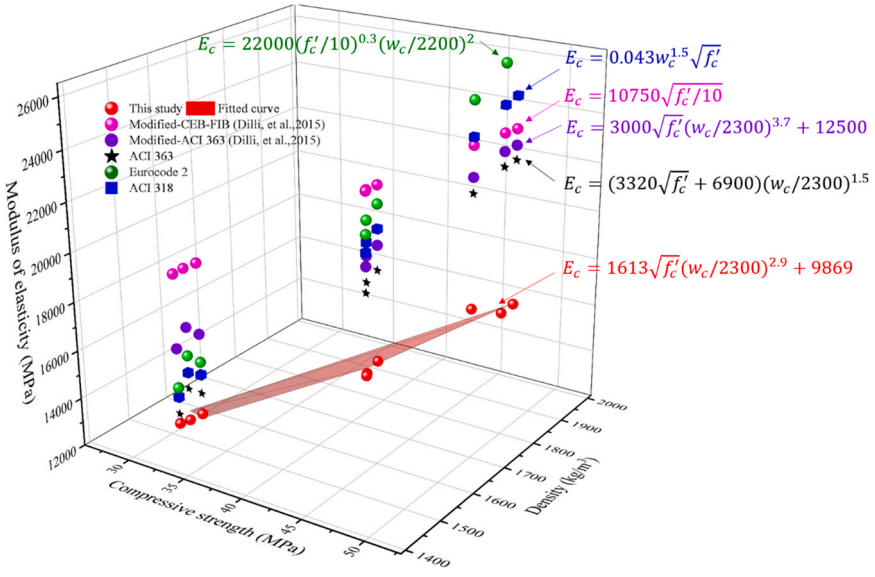

Fig. 12. Comparison of modulus of elasticity from this study and prediction models [68,69,71,72].

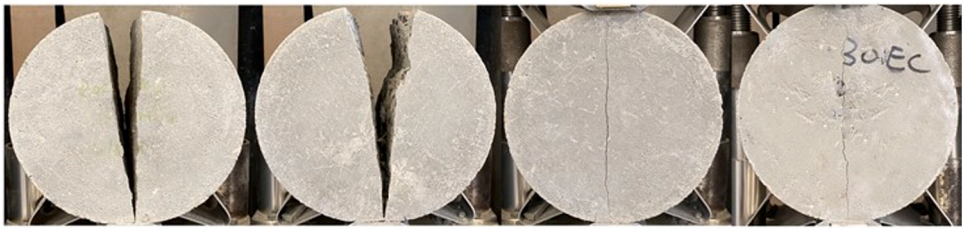

Fig. 13. Comparison of failure patterns of GM and LWGPCs under quasi-static splitting tension.

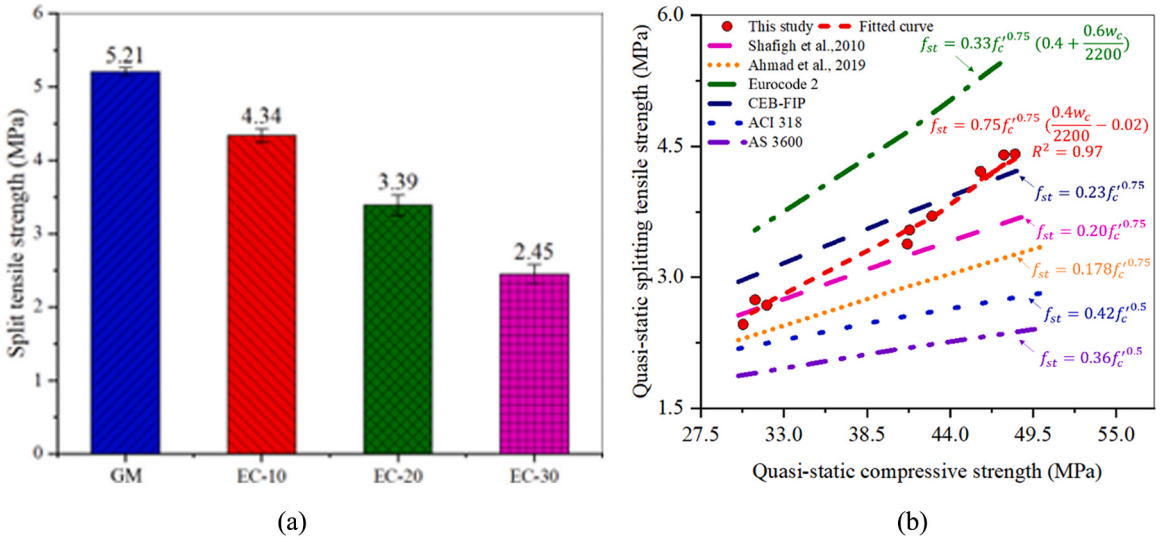

Fig. 14. Comparison of splitting tensile strength of (a) GM and LWGPCs and (b) the results of this study and the prediction models [67,70–74].

Table 4
Quasi-static test results of GM and LWGPCs.

Mixes	Density (SD) (kg/m^3)	Compressive strength (SD) (MPa)	Splitting tensile strength (SD) (MPa)	Modulus of elasticity (SD) (GPa)	Poisson's ratio (SD)	Flow rate (%)
GM	2204 (40)	61.12 (1.17)	5.21 (0.05)	17.82 (0.71)	0.11 (0.01)	104.33
EC-10	1909 (21)	48.55 (0.95)	4.34 (0.09)	16.04 (0.16)	0.14 (0.05)	96.67
EC-20	1719 (16)	40.81 (0.21)	3.39 (0.24)	13.44 (0.25)	0.16 (0.02)	88.33
EC-30	1529 (20)	31.1 (0.64)	2.45 (0.13)	11.65 (0.25)	0.19 (0.03)	80.35

Note: SD = standard deviation.

investigation. Fig. 15 presents typical SEM micrographs of LWGPC. The ITZ was well-defined due to the distinct microstructures of EC and the geopolymer matrix. Compact microstructures were observed in the geopolymer matrix for all mixtures. The geopolymer matrix and EC exhibited strong bonding without noticeable gaps or pore-line cracks between the EC and mortar. This observation explains the relatively high compressive strength of LWGPCs with EC found in this study. Furthermore, the volume fraction change of EC content in LWGPCs had no significant influence on the ITZ bonding between the geopolymer matrix and EC. With regard to the high water-to-binder ratio, the bond between the aggregate and geopolymer matrix was weakened due to the accumulation of a higher amount of water at the ITZ. In contrast, a relatively lower activator-to-binder ratio of 0.4 was applied in this study. EC, as porous clay aggregates, had high water absorption, which further reduced the influence of water content. Moreover, as observed, slurry shrinkage can generate voids within the geopolymer matrix during the casting and curing processes, as shown in Fig. 15.

4. Dynamic compressive properties

4.1. Failure progress and failure mode

Fig. 16 (a)–(d) show the typical failure progression of all configurations of specimens. The reference time of 0 μs is aligned with the moment when the specimen first encounters stress from the pressure bars. The cracks were marked in yellow for visualization. Surface cracks initially formed at peripheries of the specimens and then propagating towards the centre. This progression indicated the attainment of stress equilibrium within the tested specimens. An increase in EC content was noted to delay the onset of surface cracks, but it resulted in earlier failure with a higher number of cracks. For instance, the GM specimen exhibited three distinct cracks at 150 μs and broken to fragment in time interval of 425 μs. In contrast, the specimen with 10 % EC (EC-10) demonstrated seven cracks at 175 μs with failure occurring at 400 μs. Four cracks appeared on the surface of the EC-20 specimen at 175 μs,

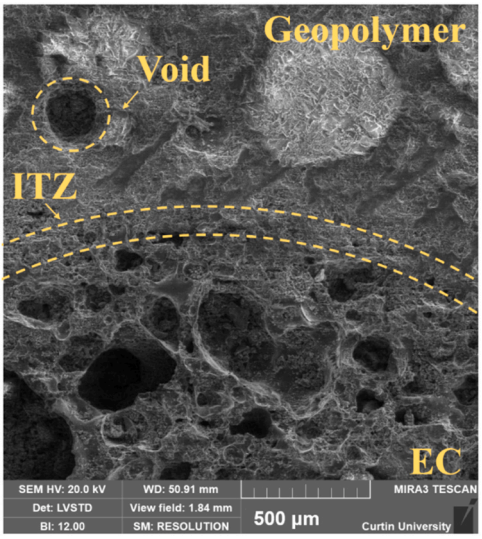

Fig. 15. SEM morphology of typical ITZ between the geopolymer matrix and EC in LWGPC.

and then the specimen failed at 375 µs. Increasing the EC content further, the EC-30 specimen (30 % EC) developed six surface cracks at 200 µs, ultimately leading to its fragmentation at 375 µs. This observed delay in the initiation of cracks can be attributed to the improved deformability by replacing sand with EC in LWGPCs.

Fig. 17 (a)–(d) show the failure patterns of representative specimens after the dynamic compressive test. As shown, the level of damage and degradation in each specimen intensified with the rising strain rate. For instance, the EC-10 specimen remained intact with cracks and slight spalling on the surface at a lower strain rate (e.g., 31.12 s^{-1}). This is because there was sufficient time to allow for stress redistribution under low strain rates. As the strain rate increased, such as 61.84 s^{-1}, the specimen was damaged, leaving a residual core with some large-sized fragments. The material could not accommodate the rapidly applied load, leading to localized failure. When the strain rate rose to 135.48 s^{-1}, the specimen was completely shattered into fragments. The failure mode of LWGPCs aligned with the experimental results from previous studies on concrete and geopolymer materials [78–80]. LWGPC is a heterogeneous material comprised of the geopolymer matrix, silica sand, and EC. It is worth noting that EC, being a porous lightweight aggregate, contains inherent voids and discontinuities. Additionally, during the casting and curing processes, slurry shrinkage can generate internal discontinuities including microcracks and voids within the matrix, as well as in the ITZ between the EC and matrix. Under static or lower strain rates, the specimen experienced visible cracks or broke into larger pieces. This is because cracks originated from existing cracks and spread through the specimen's relatively weaker sections. However, when subjected to higher strain rates, an increased number of cracks originated from internal discontinuities. This was evidenced by a significant increase in the number of smaller fragments.

As the content of EC increased, the destruction of specimens was more severe at similar strain rates. For instance, the EC-10 specimen experienced edge crushing with the core remaining intact at a strain rate of 61.84 s^{-1}. In contrast, the EC-30 specimen disintegrated into small pieces at a slightly lower strain rate of 59.52 s^{-1}. This difference in failure modes can be ascribed to the porous nature of EC, which diminishes the compressive strength and alters the failure mechanisms under high strain rate loading. The EC particles and the ITZ between the EC and the matrix were weaker compared to the matrix itself. As a result, there were more internal cracks that originated from inherent microcracks and voids within the EC, generating a higher quantity of smaller fragments. This phenomenon was similarly observed in a previous study on concrete-like materials [35]. Therefore, under a high strain rate, faster development of more microcracks into main cracks occurred.

4.1.1. Stress-strain curves

The compressive stress–strain curves for each configuration at various strain rates are shown in Fig. 18 (a)–(d). Initially, the stress-strain curves of all mixtures ascended steeply and linearly, signifying the elastic compression of the specimens under dynamic loading. Following this, the upward trajectory of the curves moderated with a lower slope, indicating that the specimens experienced damage due to microcracks. The stress-strain curves subsequently transitioned into a plateau phase, characterized by constant stress levels despite increasing strain. This is because micro-voids in the specimens underwent significant compression, leading to an accumulation of damage. Thereafter, the stress declined as the strain continued to increase until reaching the maximum strain. Notably, a reduction in strain was observed at the tail end of the stress-strain curves at strain rates around 30 s^{-1}. This phenomenon can be attributed to the compression of the input bar by either the intact specimen or its residual cone following unloading expansion recovery [47], causing an approximately linear-elastic unloading pattern in the stress-strain curves towards the tail end. As the strain rate increased, this phenomenon diminished due to the specimens incurring more extensive damage. A similar phenomenon was observed in previous studies [35,81].

When subjected to higher strain rates, there was a noticeable increasing trend in the dynamic compressive strength of LWGPCs. The compressive strength of EC-10 increased from 70.2 to 132.4 MPa as the strain rate rose from 31.12 to 138.21 s^{-1}, indicating that LWGPCs with EC are strain-rate-dependent. As elaborated in Section 4.1.1, an increase in strain rate led to specimen failure through the creation and spread of more internal cracks, resulting in a larger number of fragments. Therefore, based on the work-energy and impulse-momentum theories, the specimens of LWGPCs could absorb more external energy and impulse [79], which improves the compressive strength under impact loading.

4.1.2. Strain rate effect on dynamic compressive properties

The dynamic increase factor for compressive strength (CDIF) is determined by normalizing the dynamic compressive strength against the quasi-static compressive strength. This factor serves to quantify the effect of strain rate on the material properties. In high-speed impact tests, the lateral inertial confinement contributes to the strength increment. However, the contribution should be excluded from the calculation because this increase is not a material property. Previous studies have quantitatively investigated the contribution of lateral inertial confinement to concrete-like materials at various strain rates [82,83]. For instance, the inertia of Ø100 × 50mm specimens was responsible for a 4–13 % strength enhancement at strain rates between 30 and 200 s^{-1}. In the current study, the CDIF of the material was determined by deducting the influence of lateral inertial confinement from the experimental CDIF.

The CDIF for the developed LWGPCs is compared in Fig. 19. As observed, LWGPC with a higher volume fraction of EC exhibited higher sensitivity to strain rate. For example, the CDIF of EC-10 increased from 1.35 to 2.40 at strain rates ranging from 31.12 to 138.21 s^{-1}, whereas the CDIF increased from 1.59 to 2.75 at strain rates of 32.5–131.35 s^{-1} when the EC content was 30 %. As illustrated in Section 4.1.1, LWGPC specimens with a higher content of EC disintegrated into a larger number of smaller fragments under similar strain rates. More external energy was dissipated by the formation and spread of more cracks, which in turn improved the compressive strength. Moreover, the internal resistance provided by the air voids trapped within the EC's porous structures, coupled with the viscosity effect caused by its restrained internal pore, further contributed to the strength increment of LWGPCs.

The empirical formulae of the relation between CDIF and the strain rate of LWGPCs based on the results in this study are provided as follows.

For EC-10:

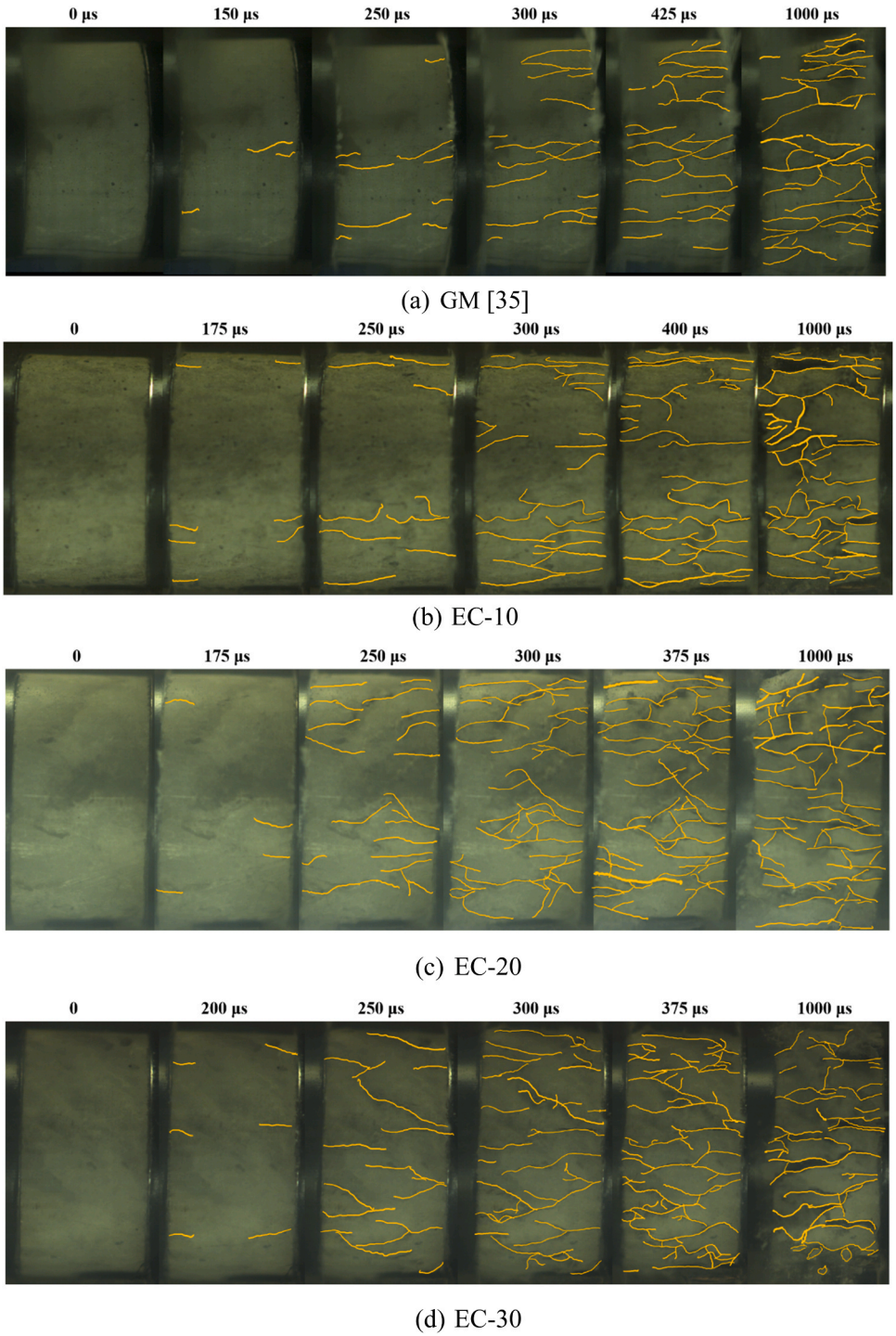

Fig. 16. Failure progress of representative specimens under compression at the strain rate of about 130 s^{-1}.

$$\mathrm{CDIF} = 0.738\ln(\dot{\varepsilon}) - 0.919,\ 31.12s^{-1} \le \dot{\varepsilon} \le 138.21s^{-1}\ (R^2 = 0.93) \quad (12)$$

For EC-20:

$$\mathrm{CDIF} = 0.652\ln(\dot{\varepsilon}) - 0.736,\ 32.10s^{-1} \le \dot{\varepsilon} \le 141.00s^{-1}\ (R^2 = 0.91) \quad (13)$$

For EC-30:

$$\mathrm{CDIF} = 0.688\ln(\dot{\varepsilon}) - 1.037,\ \text{for } 32.50\,s^{-1} \le \dot{\varepsilon} \le 131.35s^{-1}\ (R^2 = 0.95) \quad (14)$$

Fig. 20 compares the CDIF of developed LWGPCs with the results from previous studies on LWC and LWGPCs. It is evident that the increasing trend of CDIF with the strain rate for LWGPCs with EC aligns with previous findings. Notably, the CDIF of all LWGPCs with EC was higher than those reported for LWC containing rubber powder ($f_c^{'}$ = 37 and 43 MPa) [84], LWC with expanded shale ($f_c^{'}$ = 50 MPa and 60 MPa) [85], and LWGPC with rubber particles ($f_c^{'}$ = 54 MPa) [86]. Additionally, LWGPCs with various EC contents had higher CDIF values than the value recommended by CEB-FIB for OPC with equivalent compressive strength [70]. LWC and LWGPC are heterogeneous materials comprising aggregates, matrix, and ITZ between the aggregate and matrix, which

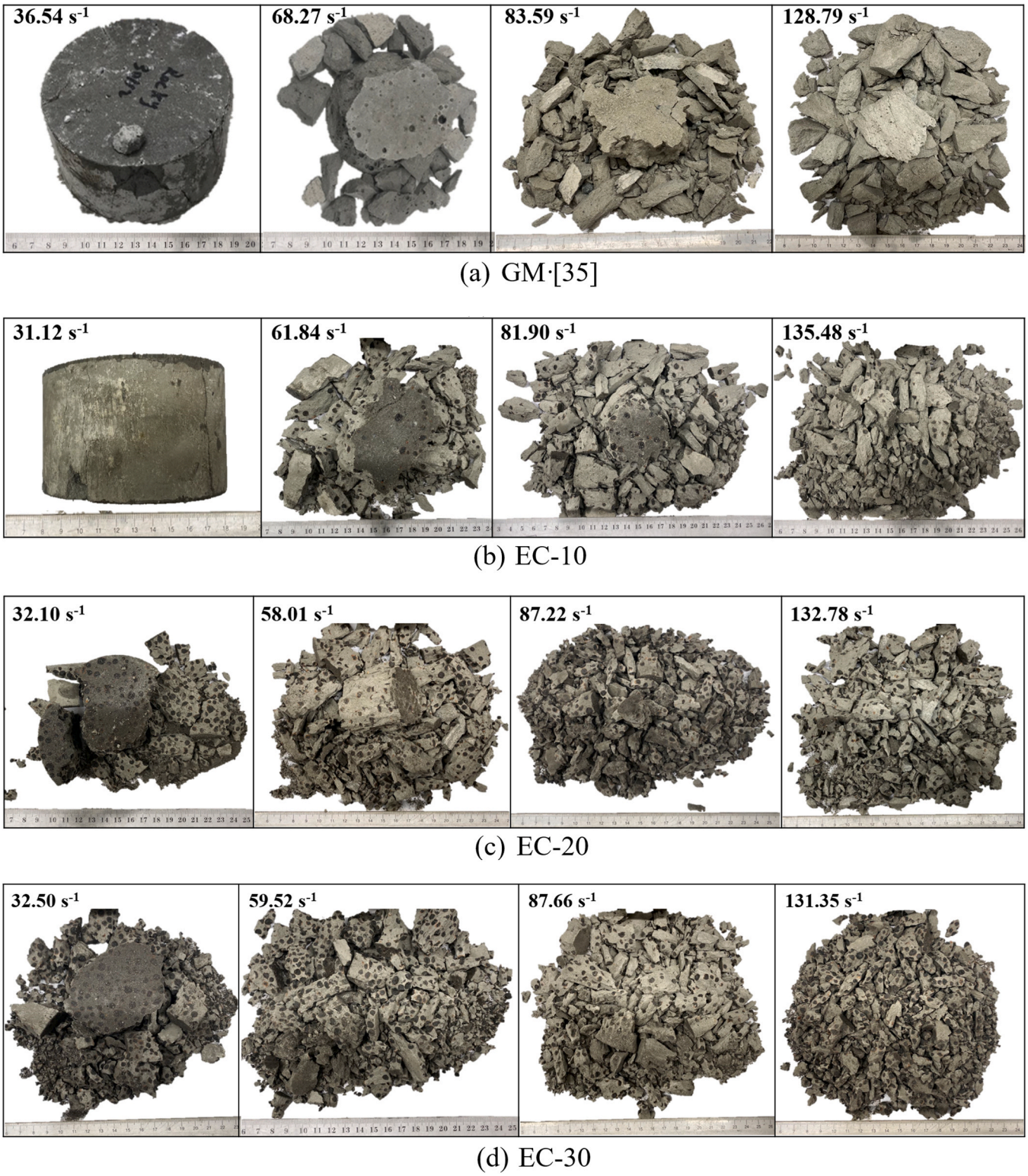

Fig. 17. Post-failure modes of GM and LWGPCs at the strain rate around 130 s^{-1}.

contributed to these differences. As demonstrated, the increased number of generated cracks and the viscosity effect from the confined voids induced by the EC particles contributed to the increase in CDIF under dynamic compression.

The critical strain refers to the axial strain at peak stress. Fig. 21 shows the effect of strain rate on the critical strain of developed LWGPCs. An increase in the critical strain for all mixtures was observed with the rising strain rate. For instance, the critical strain for EC-20 rose from 0.15 % to 0.41 % with an increasing strain rate. This upward trend aligns with findings from previous studies [34,49,87,88]. However, some other studies have reported different observations on critical strain with strain rate, namely decreasing trends in [89,90] or unchanged in [91]. Therefore, further research is necessary to affirm the influence of strain rate on the critical strain of geopolymer composites.

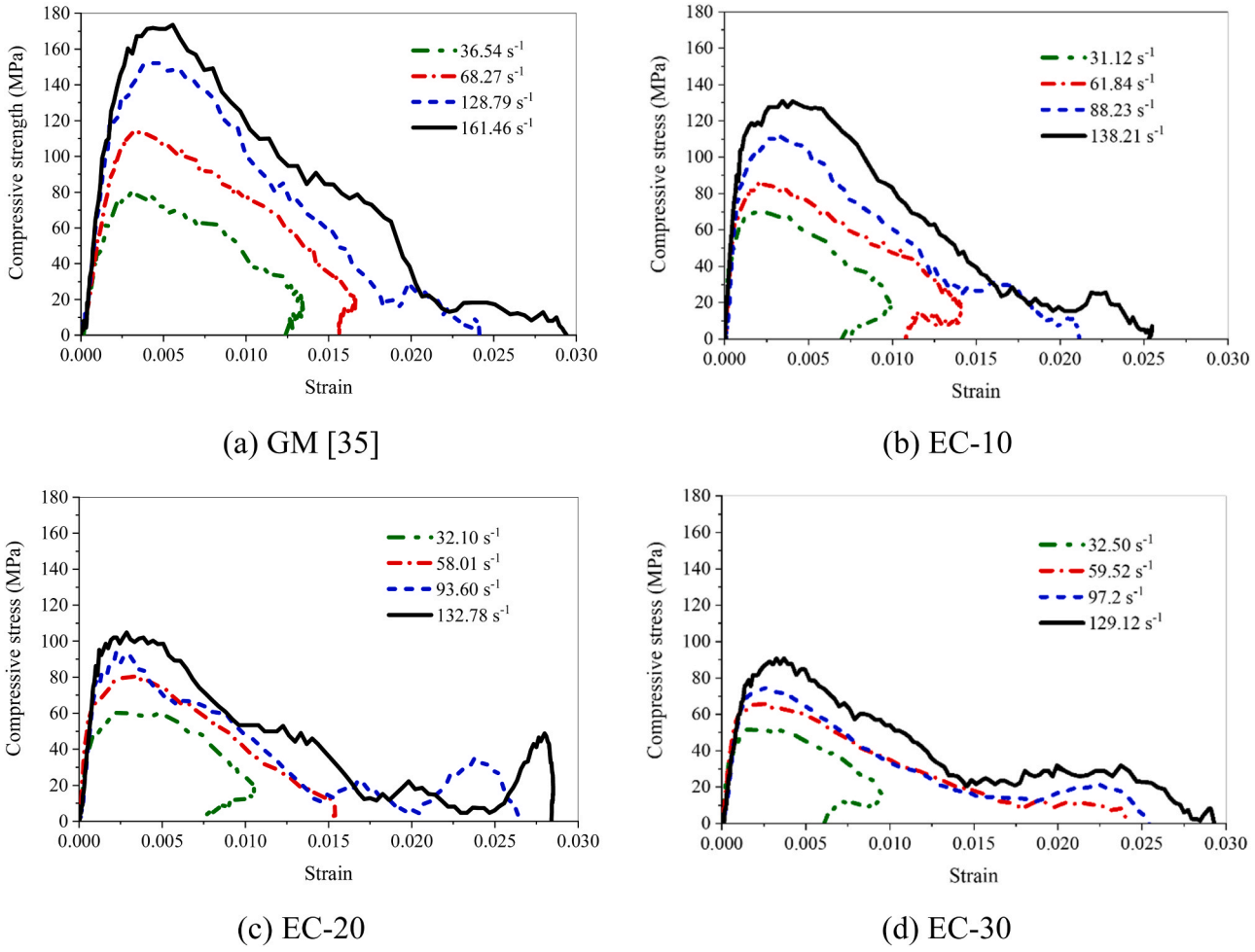

Fig. 18. Dynamic compressive stress-strain curves of GM and LWGPCs with various contents of EC.

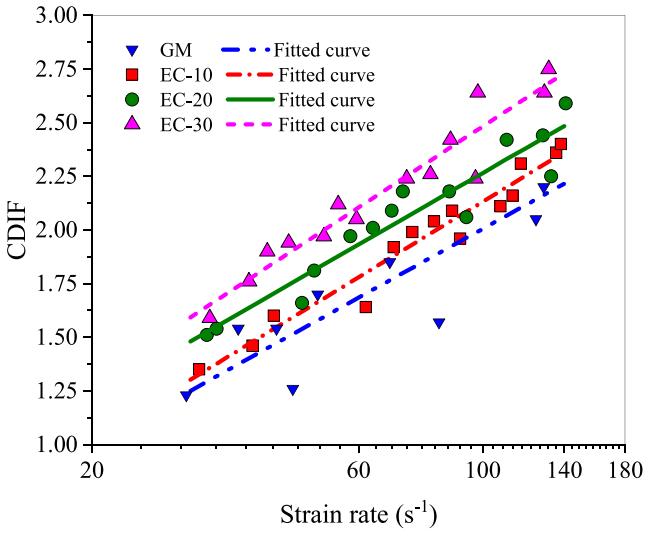

Fig. 19. Comparison of CDIF under different strain rates.

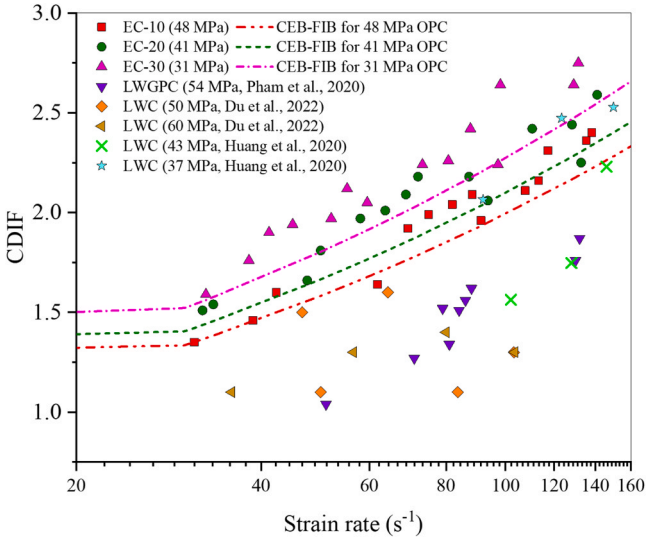

Fig. 20. Comparison of CDIF of developed LWGPC with previous studies.

4.1.3. Energy absorption

The capacity of a material to absorb energy, termed as toughness, can be evaluated using strain energy density (U). The U value is determined by calculating the area under the stress-strain curves. Fig. 22 (a) presents the energy absorption capacities of LWGPCs at various strain rates. As depicted, all mixtures demonstrated an upward trend in energy absorption with an increased strain rate. Specifically, the strain energy density of EC-10 increased from 513.13 to 1746.24 kJ/m^3 as the strain rate rose from 31.12 s^{-1} to 138.21 s^{-1}. This enhancement is attributed to the initiation of more microcracks and fracture surfaces at higher

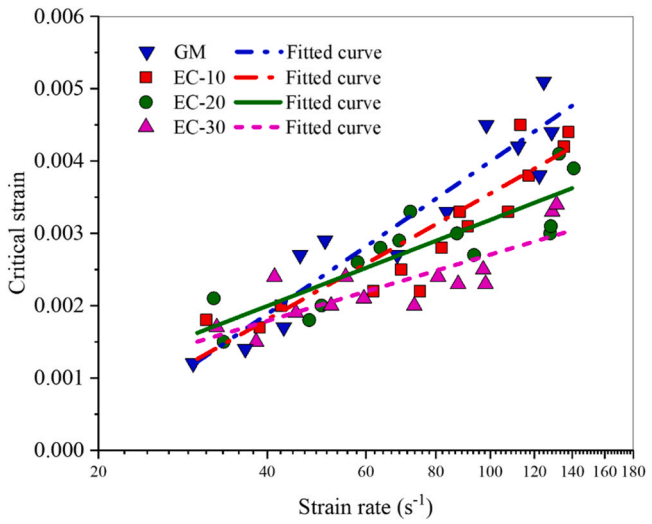

Fig. 21. Comparison of critical strain under different strain rates.

strain rates, as illustrated in Fig. 17. The strain energy density of LWGPCs with EC exhibited significant sensitivity to variations in strain rate.

The relationship of U against the corresponding range of strain rate ($\dot{\varepsilon}$) for the specimens can be expressed as follows.

For EC-10:

$$U = -0.001\dot{\varepsilon}^2 + 13.74\dot{\varepsilon} + 45.57 \text{ for } 31.12 s^{-1} \le \dot{\varepsilon} \le 138.21\ s^{-1}\ (R^2 = 0.96) \quad (15)$$

For EC-20:

$$U = -0.020\dot{\varepsilon}^2 + 12.51\dot{\varepsilon} + 84.67 \text{ for } 32.10\ s^{-1} \le \dot{\varepsilon} \le 141.00 s^{-1} (R^2 = 0.93) \quad (16)$$

For EC-30:

$$U = -0.025\dot{\varepsilon}^2 + 12.59\dot{\varepsilon} - 30.57 \text{ for } 32.50\ s^{-1} \le \dot{\varepsilon} \le 131.35\ s^{-1}\ (R^2 = 0.96) \quad (17)$$

However, LWGPC with a higher percentage of EC had lower strain energy density. At the strain rate of around 30 s^{-1}, the strain energy density of GM was 711.90 kJ/m^3, which decreased by 27.92 %, 30.28 %, and 51.24 % with EC contents of 10 %, 20 %, and 30 %, respectively. When subjected to the strain rate around 130 s^{-1}, the U value of GM was 2783.44 kJ/m^3, which was reduced by 38.84 %, 47.66 % and 57.36 % for EC-10, EC-20 and EC-30, respectively. This is because the strain energy density as a composite index is derived from both intrinsic strength and ductility. The specific energy absorption capacities (SEAC) can assess the influence of EC on the energy absorption capacities of LWGPCs with different strengths. SEAC were determined by normalizing the strain energy density by the quasi-static compressive strength. Fig. 22(b) illustrates the comparison of specific SEAC of developed LWGPCs and GM. It was noted that the SEAC of both the GM and the developed LWGPCs under dynamic compression exhibited an approximate linear increase in relation to the strain rate. The SEAC of GM was generally higher than that of LWGPC. It might be because the influence of strength on the strain energy density was enhanced with the rising strain rate. It is worth noting that the SEAC of EC-30 was higher than that of EC-10 and EC-20. For instance, at the strain rate around 87 s^{-1}, the SEAC of LWGPCs with the EC percentage of 10 %, 20 % and 30 % was 24.39, 26.95 and 29.62 kJ/m^3/MPa, respectively. The dynamic compressive strength, CDIF, critical strain, strain energy density and specific energy absorption of all configurations of specimens are summarised in Table 5-Table 7.

5. Dynamic splitting tensile properties

5.1. Fracture process and failure pattern

Fig. 23 (a)–(d) depict the fracture progress at various time instants for GM and LWGPCs. The cracks originated from the centre of all the specimens, where the peak tensile stress was reached. As observed, all specimens were fractured into two halves due to the development of a major crack. For GM, the main crack was generated at 233 μs and extended throughout the specimen along its diameter by 266 μs. In contrast, for LWGPCs with EC contents of 10 %, 20 %, and 30 %, the primary crack was generated earlier and expanded faster throughout the specimens. This can be attributed to the reduced effective stress area and the increased number of internal microcracks with the increase in EC content.

Fig. 24 presents the failure mode of specimens under strain rates around 6 s^{-1} to 10 s^{-1}. As shown, the triangular damage zone was located at the loading ends in all specimens. The extent of this crushed zone expanded as the strain rate increased. This is in line with the

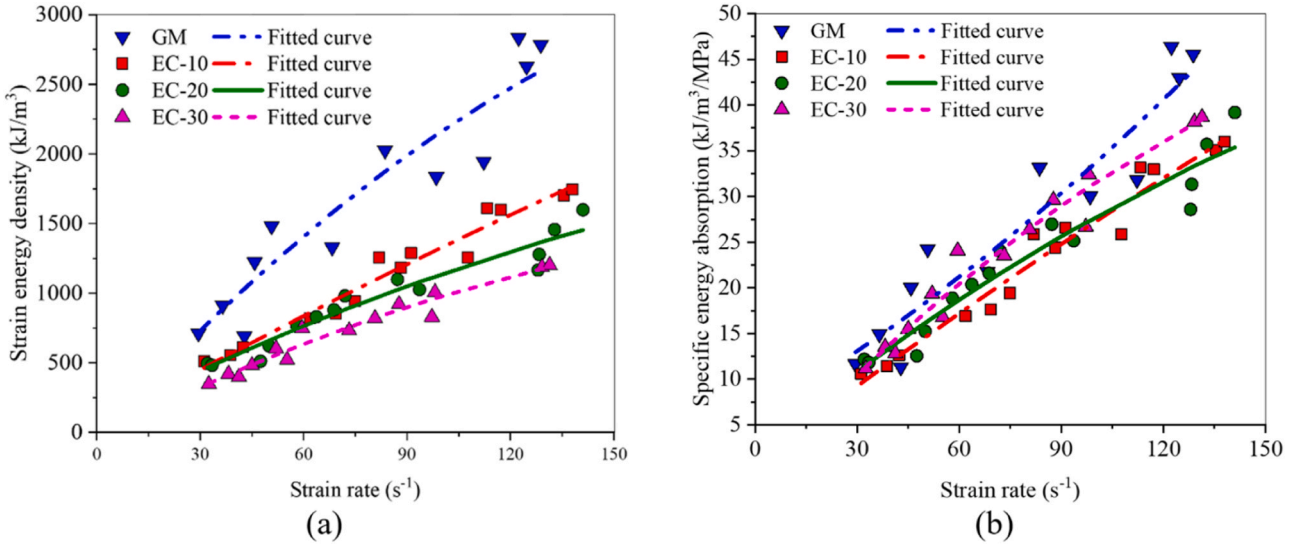

Fig. 22. Comparison of (a) strain energy density and (b) specific energy absorption capacities under different strain rates.

Table 5
Results of dynamic compressive test results for EC-10.

Specimen	Strain rate (s^{-1})	Dynamic compressive strength (MPa)	ECDIF	CDIF	Critical strain (%)	Energy absorption (kJ/m^3)	Specific energy absorption (kJ/m^3/MPa)
EC-10–1	31.12	70.2	1.45	1.35	0.18	513.13	10.57
EC-10–2	38.79	76.3	1.57	1.46	0.17	554.26	11.42
EC-10–3	42.33	83.8	1.73	1.60	0.2	612.54	12.62
EC-10–4	61.84	86.9	1.79	1.64	0.22	819.77	16.89
EC-10–5	69.32	96.8	1.99	1.92	0.25	855.54	17.62
EC-10–6	74.89	106.2	2.19	1.99	0.22	942.68	19.42
EC-10–7	81.90	109.3	2.25	2.04	0.28	1256.32	25.88
EC-10–8	88.23	112.4	2.31	2.09	0.33	1183.91	24.39
EC-10–9	91.2	105.6	2.17	1.96	0.31	1289.66	26.56
EC-10–10	107.64	114.6	2.36	2.11	0.33	1255.66	25.86
EC-10–11	113.22	117.7	2.42	2.16	0.45	1609.72	33.16
EC-10–12	117.23	120.7	2.49	2.31	0.38	1599.99	32.96
EC-10–13	135.48	121.8	2.51	2.36	0.42	1702.3	35.06
EC-10–14	138.21	132.4	2.73	2.40	0.44	1746.24	35.97

Note: ECDIF is the experimental results of DIF of compressive strength, CDIF is the true DIF of compressive strength.

Table 6
Results of dynamic compressive test results for EC-20.

Specimen	Strain rate (s^{-1})	Dynamic compressive strength (MPa)	ECDIF	CDIF	Critical strain (%)	Energy absorption (kJ/m^3)	Specific energy absorption (kJ/m^3/MPa)
EC-20–1	32.10	66.09	1.62	1.51	0.21	496.28	12.16
EC-20–2	33.42	67.45	1.65	1.54	0.15	482.24	11.82
EC-20–3	47.52	73.32	1.80	1.66	0.18	511.58	12.54
EC-20–4	50.00	80.07	1.96	1.81	0.2	621.22	15.22
EC-20–5	58.01	87.55	2.15	1.97	0.26	769.72	18.86
EC-20–6	63.71	89.62	2.20	2.01	0.28	830.71	20.36
EC-20–7	68.80	89.43	2.19	2.09	0.29	880.58	21.58
EC-20–8	72.00	89.15	2.18	2.18	0.33	980.65	24.03
EC-20–9	87.22	94.87	2.32	2.18	0.3	1100	26.95
EC-20–10	93.60	93.38	2.29	2.06	0.27	1026.26	25.15
EC-20–11	110.51	103.82	2.54	2.42	0.3	1166.39	28.58
EC-20–12	128.32	109.85	2.69	2.44	0.31	1278.66	31.33
EC-20–13	132.78	104.08	2.55	2.25	0.41	1456.86	35.70
EC-20–14	141.00	116.11	2.85	2.59	0.39	1599.24	39.19

Table 7
Results of dynamic compressive test results for EC-30.

Specimen	Strain rate (s^{-1})	Dynamic compressive strength (MPa)	ECDIF	CDIF	Critical strain (%)	Energy absorption (kJ/m^3)	Specific energy absorption (kJ/m^3/MPa)
EC-30–1	32.50	53.20	1.71	1.59	0.17	347.15	11.16
EC-30–2	38.20	59.09	1.89	1.76	0.15	420.56	13.52
EC-30–3	41.20	63.90	2.05	1.9	0.24	398.56	12.82
EC-30–4	45.00	65.40	2.10	1.94	0.19	482.22	15.51
EC-30–5	52.00	66.68	2.14	1.97	0.2	601.98	19.36
EC-30–6	55.20	71.89	2.30	2.12	0.24	521.63	16.77
EC-30–7	59.52	69.69	2.23	2.05	0.21	748.98	24.08
EC-30–8	73.20	75.71	2.43	2.24	0.2	731.63	23.53
EC-30–9	80.70	76.72	2.46	2.26	0.24	820.66	26.39
EC-30–10	87.66	81.85	2.62	2.42	0.23	921.24	29.62
EC-30–11	97.20	77.75	2.49	2.24	0.25	829.61	26.68
EC-30–12	98.10	81.96	2.63	2.64	0.23	1008.23	32.42
EC-30–13	129.12	93.16	2.99	2.64	0.33	1186.76	38.16
EC-30–14	131.35	97.15	3.11	2.75	0.34	1202.54	38.67

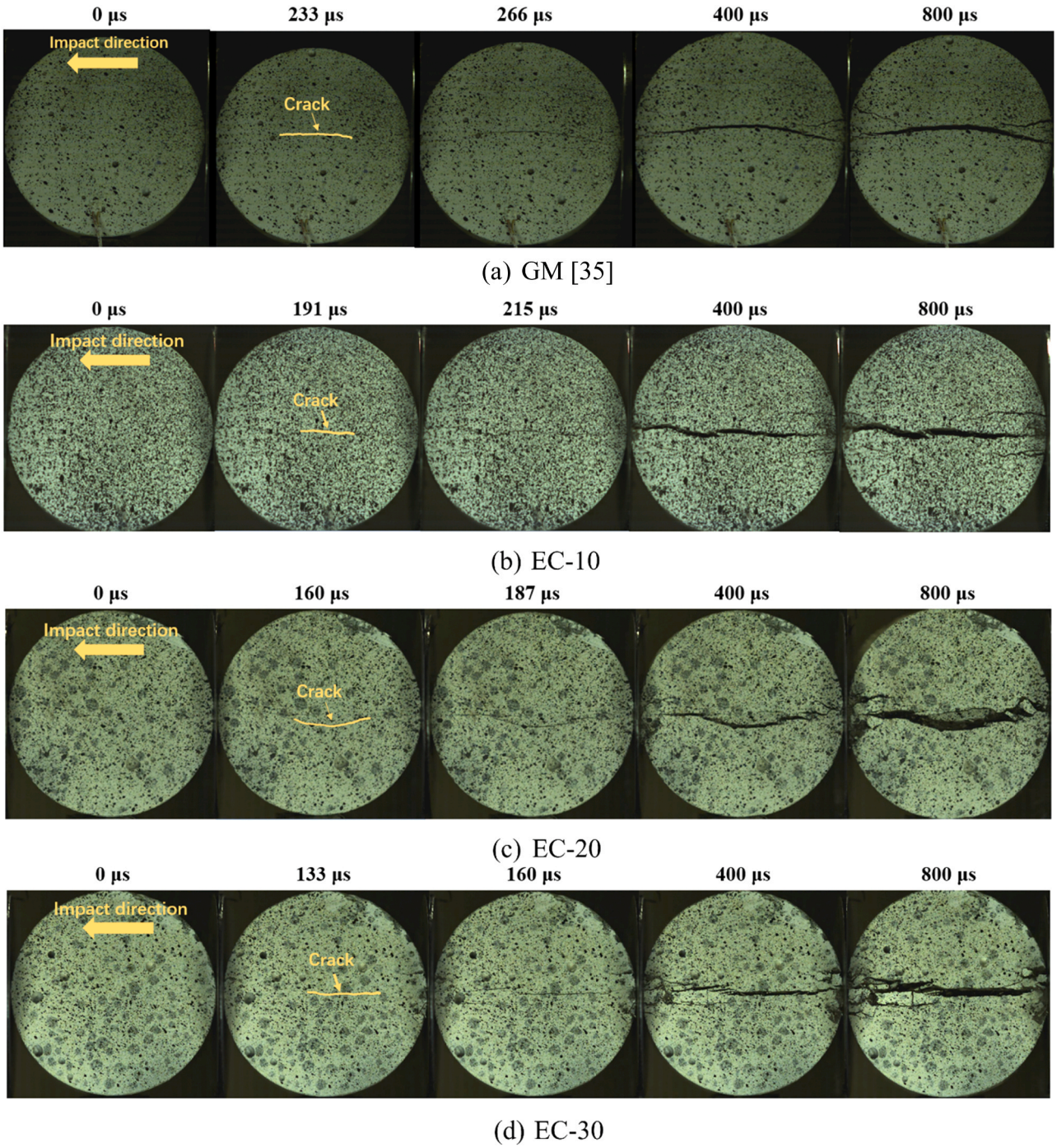

Fig. 23. Illustration of failure process of representative specimens under splitting tension at the strain rate around 6 s^{-1}.

findings from previous research on concrete-like materials [92]. The cracks were generated from microcracks existed in the matrix, voids in the EC particles and ITZ between EC and matrix under dynamic split tension.

5.1.1. Stress vs. time and COD

Fig. 25 (a)–(d) show time-dependent progression of the dynamic strength of LWGPCs under split tension. As shown, a rise in strain rate led to an increase in the peak splitting tensile strength for all mixtures. For example, the dynamic splitting tensile strength of EC-10 increased from 9.20 MPa to 16.49 MPa as the strain rate rose from 5.28 s^{-1} to 10.36 s^{-1}. This trend aligns with the findings from previous research on geopolymer composites [92–94]. This is mainly because that more cracks were generated and developed at higher strain rates. COD time histories at the strain rate of approximately 10 s^{-1} were recorded, as shown in Fig. 26. The COD was found to increase with the increasing EC content. For instance, at 0.001 s, the COD of GM, EC-10, EC-20 and EC-30 were 3.90 mm, 5.16 mm, 6.08 mm, and 7.07 mm, respectively. This increase can be attributed to the reduced effective stress area and the increased number of internal microcracks with the increase in EC content.

5.1.2. Strain rate effect on dynamic splitting tensile properties

DIF for the splitting tensile strength (TDIF) can be utilized to evaluate the sensitivity of the strength of LWGPCs to strain rate under split tension. The results of TDIF against strain rates are plotted in Fig. 27.

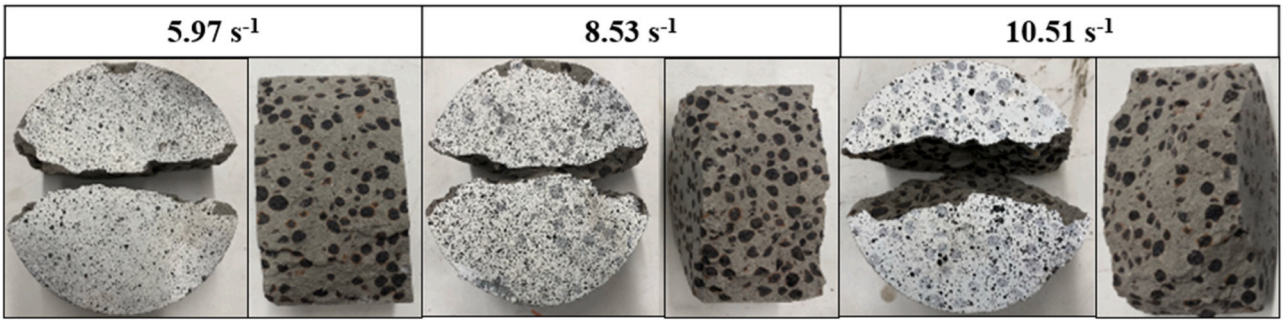

Fig. 24. Typical failure pattern of LWGPCs under dynamic split tension.

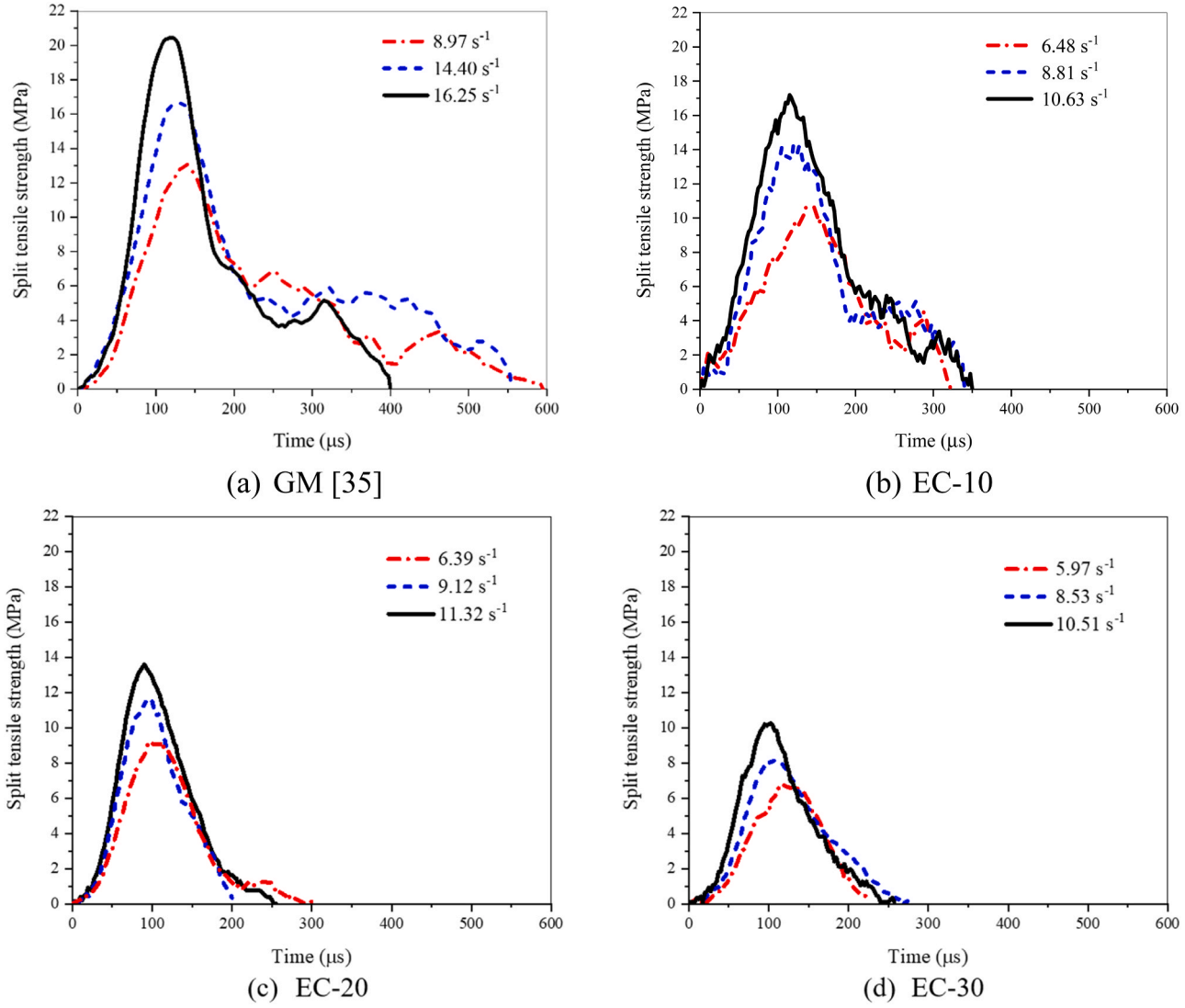

Fig. 25. Time-dependent progression of the dynamic splitting tensile strength.

With the increasing strain rate, a rising trend in TDIF of LWGPCs was observed. For instance, the TDIF of EC-20 increased from 3.00 to 4.01 as the strain rate rose from 6.39 s^{-1} to 11.32 s^{-1}. It is worth noting that LWGPCs exhibited higher sensitivity to strain rate in comparison to GM. Moreover, with an increasing volume fraction of EC, this sensitivity became even more pronounced, i.e., the TDIF was 3.78 for EC-30 at the strain rate of 9.12 s^{-1}, 3.08 for EC-10 at the strain rate of 9.21 s^{-1} and 2.77 for GM at the strain rate of 11.24 s^{-1}, respectively. The empirical formulae of the relationship between TDIF and the strain rate of LWGPCs based on the results in this study are provided as follows.

For EC-10:

$$\mathrm{TDIF} = 1.796\ln(\dot{\varepsilon}) - 0.7326 \text{ for } 5.28\ s^{-1} \le \dot{\varepsilon} \le 10.64\ s^{-1}\ (R^2 = 0.88) \tag{18}$$

For EC-20:

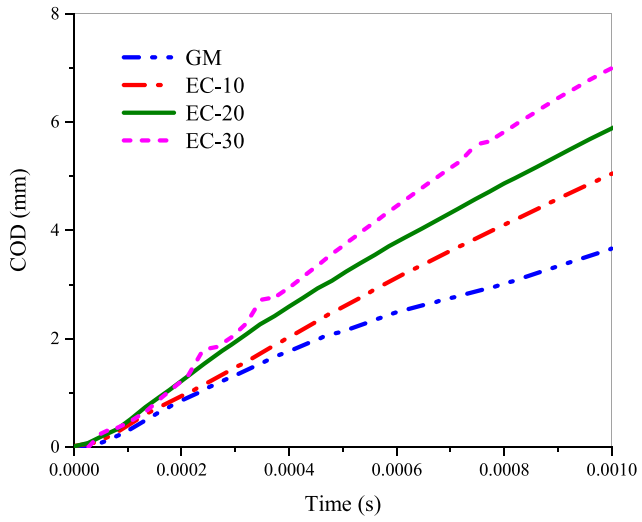

Fig. 26. Time histories of the COD at the strain rate of approximately 10 s^{-1}.

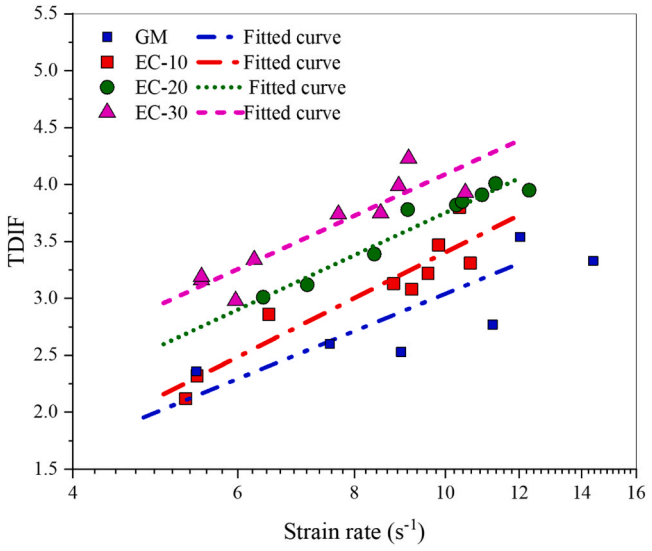

Fig. 27. Comparison of TDIF under different strain rates.

$$\text{TDIF} = 1.6539\ln(\dot{\varepsilon}) - 0.0560 \text{ for } 6.39\ s^{-1} \le \dot{\varepsilon} \le 12.3\ s^{-1}\ (R^2 = 0.94) \quad (19)$$

For EC-30:

$$\text{TDIF} = 1.6329\ln(\dot{\varepsilon}) - 0.3311 \text{ for } 5.49\ s^{-1} \le \dot{\varepsilon} \le 10.51\ s^{-1}\ (R^2 = 0.84) \quad (20)$$

The dynamic split tensile strength and TDIF of all configurations of specimens are summarised in Table 8–Table 10.

6. Conclusion

In this study, the novel ambient-cured lightweight geopolymer composites (LWGPCs) were developed using expanded clay (EC) as lightweight aggregate (LWA) in contents of 10 %, 20 %, and 30 % by volume. The physical properties of LWGPC with different EC contents, including microstructure, density and workability were investigated. The influence of EC contents on the quasi-static mechanical properties of LWGPCs, such as compressive strength, splitting tensile strength, modulus of elasticity and Poisson's ratio, were studied. Empirical formulae for predicting the static compressive and splitting tensile strength, as well as the modulus of elasticity of the developed LWGPCs with EC were proposed. The dynamic properties including both compression and split tension of LWGPCs with different EC contents were also investigated with the strain rate in the range of 31.12–141 s^{-1} for dynamic compressive loading and 5.28–12.30 s^{-1} for dynamic splitting tensile loading, respectively. The main findings in this study are summarized as follows:

1. The developed ambient-cured LWGPCs with three contents of EC meet the requirement of structural concrete [56,65]. The developed LWGPCs exhibited a superior strength-to-weight ratio compared to those of LWC and LWGPCs with EC reported in previous studies. This enhancement is attributed to the use of fly ash combined with an optimal quantity of slag as the binder, which significantly improves the geopolymer matrix's microstructural compactness and the bond strength between the EC and the matrix.
2. The quasi-static properties of LWGPCs with EC, including compressive strength, splitting tensile strength and modulus of elasticity, reduced with more EC contents. The proposed formulae can well predict the modulus of elasticity and splitting tensile strength by using the compressive strength of LWGPCs.
3. The dynamic compressive and splitting tensile properties of LWGPCs with EC, i.e., failure modes, dynamic strength, critical strain and energy absorption capacities were sensitive to strain rates. The CDIF and TDIF of LWGPCs with higher volume fraction of EC exhibited higher sensitivity to strain rate.

Table 8
Results of dynamic splitting tensile test results for EC-10.

Specimen	Strain rate (s^{-1})	Dynamic split tensile strength (MPa)	TDIF
EC-10–1	6.48	12.41	2.86
EC-10–2	5.43	10.07	2.32
EC-10–3	5.28	9.20	2.12
EC-10–4	8.81	13.58	3.13
EC-10–5	9.59	13.97	3.22
EC-10–6	9.21	13.37	3.08
EC-10–7	10.36	16.49	3.8
EC-10–8	9.84	15.06	3.47
EC-10–9	10.64	14.37	3.31

Table 9
Results of dynamic splitting tensile test results for EC-20.

Specimen	Strain rate (s^{-1})	Dynamic split tensile strength (MPa)	TDIF
EC-20–1	6.39	10.20	3.01
EC-20–2	8.4	11.49	3.39
EC-20–3	7.12	10.58	3.12
EC-20–4	9.12	12.81	3.78
EC-20–5	10.28	12.95	3.82
EC-20–6	10.43	13.05	3.85
EC-20–7	12.3	13.39	3.95
EC-20–8	10.95	13.25	3.91
EC-20–9	11.32	13.59	4.01

Table 10
Results of dynamic splitting tensile test results for EC-30.

Specimen	Strain rate (s^{-1})	Dynamic split tensile strength (MPa)	TDIF
EC-30–1	5.49	7.74	3.16
EC-30–2	5.97	7.30	2.98
EC-30–3	5.50	7.82	3.19
EC-30–4	7.69	9.16	3.74
EC-30–5	8.53	9.19	3.75
EC-30–6	6.25	8.18	3.34
EC-30–7	8.92	9.78	3.99
EC-30–8	9.14	10.36	4.23
EC-30–9	10.51	9.63	3.93

4. Based on the experimental results, the empirical formulae were proposed for the dynamic increase factor of the compressive strength (CDIF) and the splitting tensile strength (TDIF) as well as the energy absorption capacities of LWGPCs with EC contents of 10 %, 20 % and 30 %. The proposed empirical formulae can be used to predict the static and dynamic material properties of LWGPCs in the design analysis.

CRediT authorship contribution statement

Hong Hao: Writing – review & editing, Supervision, Funding acquisition, Conceptualization. **Zhiqiang Yin:** Writing – review & editing, Methodology. **Mizan Ahmed:** Writing – review & editing. **Wensu Chen:** Writing – review & editing, Supervision, Project administration, Methodology, Conceptualization. **Zhixing Li:** Writing – original draft, Investigation, Formal analysis, Data curation, Conceptualization.

Declaration of Competing Interest

The authors declare that they have no known competing financial interests or personal relationships that could have appeared to influence the work reported in this paper.

Acknowledgements

The authors acknowledge the financial support from the Australian Research Council (ARC) via Australian Laureate Fellowship (FL180100196).

References

[1] F.U.A. Shaikh, Mechanical and durability properties of fly ash geopolymer concrete containing recycled coarse aggregates, Int. J. Sustain. Built Environ. 5 (2) (2016) 277–287.
[2] R. Liu, et al., Quantitative phase analysis and microstructural characterization of Portland cement blends with diatomite waste using the Rietveld method, J. Mater. Sci. 56 (2) (2021) 1242–1254.
[3] M.F. Junaid, et al., Lightweight concrete from a perspective of sustainable reuse of waste byproducts, Constr. Build. Mater. 319 (2022) 126061.
[4] A. Kuqo, et al., Use of dry mixing-spraying process for the production of geopolymer-bonded wood and seagrass fibreboards, Compos. Part B: Eng. 248 (2023) 110387.
[5] A. Albidah, et al., Characteristics of metakaolin-based geopolymer concrete for different mix design parameters, J. Mater. Res. Technol. 10 (2021) 84–98.
[6] F.A. Shilar, et al., Preparation and validation of sustainable metakaolin based geopolymer concrete for structural application, Constr. Build. Mater. 371 (2023) 130688.
[7] B.B. Jindal, et al., Geopolymer concrete with metakaolin for sustainability: a comprehensive review on raw material's properties, synthesis, performance, and potential application, Environ. Sci. Pollut. Res. (2022) 1–26.
[8] B. Kim, S. Lee, Review on characteristics of metakaolin-based geopolymer and fast setting, J. Korean Ceram. Soc. 57 (2020) 368–377.
[9] Y.M. Amran, et al., Clean production and properties of geopolymer concrete; a review, J. Clean. Prod. 251 (2020) 119679.
[10] F.U.A. Shaikh, Review of mechanical properties of short fibre reinforced geopolymer composites, Constr. Build. Mater. 43 (2013) 37–49.
[11] X. Luo, et al., The preparation of energy-absorbing material by using solid waste, RSC Adv. 5 (12) (2015) 9283–9289.
[12] W. Huang, H. Wang, Multi-aspect engineering properties and sustainability impacts of geopolymer pervious concrete, Compos. Part B: Eng. 242 (2022) 110035.
[13] J.-X. Lu, et al., A novel high-performance lightweight concrete prepared with glass-UHPC and lightweight microspheres: towards energy conservation in buildings, Compos. Part B: Eng. 247 (2022) 110295.
[14] B. EN 206, Concrete-Specification, performance, production and conformity, British Standards Institution, Her Majesty Stationery Office, London, United Kingdom, 2013..
[15] M.S.T. Masoule, et al., Lightweight geopolymer concrete: A critical review on the feasibility, mixture design, durability properties, and microstructure, Ceram. Int. 48 (8) (2022) 10347–10371.
[16] M. Nodehi, A comparative review on foam-based versus lightweight aggregate-based alkali-activated materials and geopolymer, Innov. Infrastruct. Solut. 6 (4) (2021) 231.
[17] M. Alexander, Engineering and transport properties of the interfacial transition zone in cementitious composites, Rilem Publications, 1999..
[18] Y.L. Sravya, et al., Effect of temperature curing on lightweight expanded clay aggregate concrete, Mater. Today.: Proc. 38 (2021) 3386–3391.
[19] A.M. Rashad, Lightweight expanded clay aggregate as a building material–an overview, Constr. Build. Mater. 170 (2018) 757–775.
[20] A. Ghamari, A. Khaloo, An innovative infill wall utilizing light expanded clay aggregate: an experimental and numerical study, Struct. Des. Tall Spec. Build. 29 (15) (2020) e1791.
[21] C. Muñoz-Ruiperez, et al., Lightweight masonry mortars made with expanded clay and recycled aggregates, Constr. Build. Mater. 118 (2016) 139–145.
[22] D. Koňáková, et al., Lime-based plasters with combined expanded clay-silica aggregate: microstructure, texture and engineering properties, Cem. Concr. Compos. 83 (2017) 374–383.
[23] A. Hassan, et al., Thermal and structural performance of geopolymer concrete containing phase change material encapsulated in expanded clay, Energy Build. 191 (2019) 72–81.
[24] M.C. Nepomuceno, et al., Mix design of structural lightweight self-compacting concrete incorporating coarse lightweight expanded clay aggregates, Constr. Build. Mater. 166 (2018) 373–385.
[25] R. Kumar, et al., Physico-mechanical and thermal properties of lightweight structural concrete with light expanded clay aggregate for energy-efficient buildings, in: Advances in Construction Materials and Sustainable Environment: Select Proceedings of ICCME 2020, Springer, 2021, pp. 175–185.
[26] N. Movahedi, E. Linul, Mechanical properties of light expanded clay aggregated (LECA) filled tubes, Mater. Lett. 217 (2018) 194–197.
[27] M. Priyanka, et al., Development of mix proportions of geopolymer lightweight aggregate concrete with LECA, Mater. Today: Proc. 27 (2020) 958–962.
[28] O.A. Abdulkareem, et al., Effects of elevated temperatures on the thermal behavior and mechanical performance of fly ash geopolymer paste, mortar and lightweight concrete, Constr. Build. Mater. 50 (2014) 377–387.
[29] K.-H. Yang, et al., Properties of alkali-activated mortar and concrete using lightweight aggregates, Mater. Struct. 43 (3) (2010) 403–416.
[30] B. Kanagaraj, et al., Physical characteristics and mechanical properties of a sustainable lightweight geopolymer based self-compacting concrete with expanded clay aggregates, Dev. Built Environ. 13 (2023) 100115.
[31] E.L. Bai, et al., Comparative study on the dynamic properties of lightweight porous concrete, RSC Adv. 8 (26) (2018) 14454–14461.
[32] X. Wu, et al., Damage characteristics and constitutive model of lightweight shale ceramsite concrete under static-dynamic loading, Eng. Fract. Mech. 259 (2022) 108137.
[33] Y. Du, et al., Experimental study on the dynamic behaviour of expanded-shale lightweight concrete at high strain rate, Mater. Struct. 55 (1) (2022) 1–17.
[34] Z. Li, et al., Dynamic compressive properties of novel lightweight ambient-cured EPS geopolymer composite, Constr. Build. Mater. 273 (2021) 122044.
[35] Z. Li, et al., Static and dynamic properties of novel ambient-cured lightweight geopolymer composites with fibre reinforced epoxy coated EPS aggregates, Compos. Part B: Eng. 250 (2023) 110439.
[36] ASTM, C618-19Standard specification for coal fly ash and raw or calcined natural pozzolan for use in concrete, West Conshohocken, PA, 2019.2019.
[37] Liapor, Expanded clay aggregate, https://www.liapor.com/en/downloads.html. Accessed 09/08 2023.
[38] M.Z.N. Khan, et al., Synthesis of high strength ambient cured geopolymer composite by using low calcium fly ash, Constr. Build. Mater. 125 (2016) 809–820.
[39] ASTMC330/C330M, Standard specification for lightweight aggregates for structural concrete, West Conshohocken, PA, USA, 2017 2017.
[40] ASTM, C1723-16, Standard guide for examination of hardened concrete using scanning electron microscopy, West Conshohocken, PA, 2016.
[41] ASTM, C1688-14, Standard test method for density and void content of freshly mixed pervious concrete, West Conshohocken, PA, 2014.
[42] ASTM, C1437-20, Standard test method for flow of hydraulic cement mortar, West Conshohocken, PA, 2020.
[43] ASTM, C39-18, Standard test method for compressive strength of cylindrical concrete specimens, West Conshohocken, PA, 2018.
[44] ASTM, C496-17, Standard test method for splitting tensile strength of cylindrical concrete specimens, West Conshohocken, PA, 2017.
[45] ASTM, C469-14, Standard test method for static modulus of elasticity and Poisson's ratio of concrete in compression, West Conshohocken, PA, 2014.
[46] Y. Hao, et al., Experimental confirmation of some factors influencing dynamic concrete compressive strengths in high-speed impact tests, Cem. Concr. Res. 52 (2013) 63–70.
[47] T. Lv, et al., Analysis on the waveform features of the split Hopkinson pressure bar tests of plain concrete specimen, Int. J. Impact Eng. 103 (2017) 107–123.
[48] W.W. Chen, B. Song, Split Hopkinson (Kolsky) Bar: Design, Testing and Applications, Springer Science & Business Media, 2010.
[49] T.M. Pham, et al., Dynamic compressive properties of lightweight rubberized concrete, Constr. Build. Mater. 238 (2020) 117705.
[50] Z. Yin, et al., Dynamic compressive test of gas-containing coal using a modified split hopkinson pressure bar system, Rock. Mech. Rock. Eng. 53 (2) (2020) 815–829.
[51] J.W. Tedesco, C.A. Ross, Experimental and numerical analysis of high strain rate splitting-tensile tests, Mater. J. 90 (2) (1993) 162–169.
[52] P. Rovnaník, Effect of curing temperature on the development of hard structure of metakaolin-based geopolymer, Constr. Build. Mater. 24 (7) (2010) 1176–1183.
[53] O. Gencel, et al., Replacement of natural sand with expanded vermiculite in fly ash-based geopolymer mortars, Appl. Sci. 11 (4) (2021) 1917.

[54] H. Cui, et al., Effect of lightweight aggregates on the mechanical properties and brittleness of lightweight aggregate concrete, Constr. Build. Mater. 35 (2012) 149–158.
[55] T. Alomayri, et al., Characterisation of cotton fibre-reinforced geopolymer composites, Compos. Part B: Eng. 50 (2013) 1–6.
[56] ACI, Guide for Structural Lightweight Aggregate Concrete, ACI 213R-14, Farmington Hills, MI, 2014.
[57] A.A.M. Ali, et al., Experimental study of the behavior of deep beams using light-weight structural leca concrete, Int. J. Inn. Res Sci. Eng. Tech. 5 (1) (2016) 428–436p.
[58] A.S. Ouda, A.M. Rashad, An investigation on the performance of lightweight mortar-based geopolymer containing high-volume LECA aggregate against high temperatures, Environ. Sci. Pollut. Res. (2022) 1–17.
[59] B.A. Tayeh, et al., Effect of elevated temperatures on mechanical properties of lightweight geopolymer concrete, Case Stud. Constr. Mater. 15 (2021) e00673.
[60] S. Paul, G. Babu, Mechanical properties of lightweight aggregate geo polymer concrete using lightweight expanded clay aggregate, Trans. Eng. Sci. 2 (10) (2014) 33–35.
[61] A. Bhogayata, et al., Utilization of expanded clay aggregates in sustainable lightweight geopolymer concrete, J. Mater. Cycles Waste Manag. 22 (6) (2020) 1780–1792.
[62] J. Shang, et al., Alternation of traditional cement mortars using fly ash-based geopolymer mortars modified by slag, J. Clean. Prod. 203 (2018) 746–756.
[63] M.Z.N. Khan, et al., Synthesis of high strength ambient cured geopolymer composite by using low calcium fly ash, Constr. Build. Mater. 125 (2016) 809–820.
[64] S. Puligilla, P. Mondal, Role of slag in microstructural development and hardening of fly ash-slag geopolymer, Cem. Concr. Res. 43 (2013) 70–80.
[65] CEB-FIP, Manual of design and technology Lightweight aggregate Concrete, London, 1977.
[66] J. Lee, et al., Structural behavior of durable composite sandwich panels with high performance expanded polystyrene concrete, Int. J. Concr. Struct. Mater. 12 (1) (2018) 1–13.
[67] M.R. Ahmad, et al., Investigate the influence of expanded clay aggregate and silica fume on the properties of lightweight concrete, Constr. Build. Mater. 220 (2019) 253–266.
[68] M.E. Dilli, et al., A comparison of strength and elastic properties between conventional and lightweight structural concretes designed with expanded clay aggregates, Constr. Build. Mater. 101 (2015) 260–267.
[69] ACI, 363-10 Report on high strength concrete, Farmington Hills, Michigan, 2010.
[70] CEB-FIB, Model code, CEB-FIP model code for concrete structures, London, 1990.
[71] ACI, 318-19 Building code requirements for structural concrete and commentary, Farmington Hills, Michigan, 2019.
[72] EN1992:, Eurocode 2, Design of concrete structures, London, 2004.
[73] AS, 3600:2018, Concrete structures, SAI Global, Sydney, Australia, 2018.
[74] P. Shafigh, et al., Mix design and mechanical properties of oil palm shell lightweight aggregate concrete: a review, Int. J. Phys. Sci. 5 (14) (2010) 2127–2134.
[75] M.R. Ahmad, B. Chen, Experimental research on the performance of lightweight concrete containing foam and expanded clay aggregate, Compos. Part B: Eng. 171 (2019) 46–60.
[76] J.A. Bogas, A. Gomes, Compressive behavior and failure modes of structural lightweight aggregate concrete–Characterization and strength prediction, Mater. Des. 46 (2013) 832–841.
[77] C.-C. Yang, R. Huang, Approximate strength of lightweight aggregate using micromechanics method, Adv. Cem. Based Mater. 7 (3-4) (1998) 133–138.
[78] X. Chen, et al., Experimental and modeling study of dynamic mechanical properties of cement paste, mortar and concrete, Constr. Build. Mater. 47 (2013) 419–430.
[79] M.Z.N. Khan, et al., Experimental evaluation of quasi-static and dynamic compressive properties of ambient-cured high-strength plain and fiber reinforced geopolymer composites, Constr. Build. Mater. 166 (2018) 482–499.
[80] S.-H. Xiao, et al., Dynamic properties of PVA short fiber reinforced low-calcium fly ash-slag geopolymer under an SHPB impact load, J. Build. Eng. 44 (2021) 103220.
[81] H. Zhang, et al., Effect of fibre addition on the static and dynamic compressive properties of ambient-cured geopolymer concrete, J. Build. Eng. 58 (2022) 104991.
[82] Y. Hao, et al., Numerical analysis of lateral inertial confinement effects on impact test of concrete compressive material properties, Int. J. Prot. Struct. 1 (1) (2010) 145–167.
[83] C. Wang, et al., Experimental investigations of dynamic compressive properties of roller compacted concrete (RCC), Constr. Build. Mater. 168 (2018) 671–682.
[84] Z. Huang, et al., Dynamic compressive behavior of a novel ultra-lightweight cement composite incorporated with rubber powder, Compos. Struct. 244 (2020) 112300.
[85] Y. Du, et al., Experimental study on the dynamic behaviour of expanded-shale lightweight concrete at high strain rate, Mater. Struct. 55 (1) (2022) 1–17.
[86] T.M. Pham, et al., Dynamic compressive properties of lightweight rubberized geopolymer concrete, Constr. Build. Mater. 265 (2020) 120753.
[87] G. Cusatis, Strain-rate effects on concrete behavior, Int. J. Impact Eng. 38 (4) (2011) 162–170.
[88] X. Zhang, et al., Dynamic compressive material properties of clay bricks at different strain rates, Constr. Build. Mater. 192 (2018) 754–767.
[89] X.X. Zhang, et al., Effect of loading rate on crack velocities in HSC, Int. J. Impact Eng. 37 (4) (2010) 359–370.
[90] L.L. Wang, et al., Studies on rate-dependent macro-damage evolution of materials at high strain rates, Int. J. Damage Mech. 19 (7) (2010) 805–820.
[91] S. Harsh, et al., Rate Sensitive Behavior of Cement Paste and Mortar in Compression, University of Kansas Center for Research, Inc., 1989.
[92] M.Z.N. Khan, et al., Mechanical properties and behaviour of high-strength plain and hybrid-fiber reinforced geopolymer composites under dynamic splitting tension, Cem. Concr. Compos. 104 (2019).
[93] X. Luo, J.-y Xu, Dynamic splitting-tensile testing of highly fluidised geopolymer concrete, Mag. Concr. Res. 65 (14) (2013) 837–843.
[94] D. Chen, et al., Dynamic compressive and splitting tensile response of unsaturated polyester polymer concrete material at different curing ages, Constr. Build. Mater. 177 (2018) 477–498.